

Peculiar COVID-19 effects in the Greater Tokyo Area revealed by spatiotemporal variabilities of tropospheric gases and light-absorbing aerosols

Alessandro Damiani¹, Hitoshi Irie¹, Dmitry [A. Belikov](#)¹, Shuei Kaizuka¹, Hossain Mohammed Syedul Hoque², Raul R. Cordero³

¹Center for Environmental Remote Sensing (CEReS), Chiba University, Chiba, 2638522, Japan

²Graduate School of Environmental Studies, Nagoya University, Nagoya, 4640064, Japan

³Department of Physics, Universidad de Santiago de Chile, Santiago, 3363, Chile

Correspondence to: Alessandro Damiani (alecarlo.damiani@gmail.com)

10 **Abstract.** This study investigated the spatiotemporal variabilities in nitrogen dioxide (NO₂), formaldehyde (HCHO), ozone (O₃), and light-absorbing aerosols within the Greater Tokyo Area, Japan, the most populous metropolitan area in the world. The analysis is based on total tropospheric column, partial [tropospheric](#) column (within the boundary layer), and *in situ* observations retrieved from multiple platforms and additional information obtained from reanalysis and box model simulations. This study mainly covers the 2013–2020 period, focusing on 2020, when air quality was influenced by the coronavirus 2019 (COVID-19) pandemic. Although total and partial [tropospheric](#) NO₂ columns were reduced by an average of about 10% in 2020, reductions exceeding 40% occurred in some areas during the pandemic state of emergency. Light-absorbing aerosol levels within the boundary layer were also reduced for most of 2020, while smaller fluctuations in HCHO and O₃ were observed. The significantly enhanced degree of weekly cycling of NO₂, HCHO, and light-absorbing aerosol found in urban areas during 2020 suggests that, in contrast to other countries, mobility in Japan also dropped on weekends.

15

20 We conclude that, despite the lack of strict mobility restrictions in Japan, widespread adherence to recommendations designed to limit the COVID-19 spread resulted in unique air quality improvements.

1 Introduction

Fossil fuel combustion is the dominant source of nitrogen oxides (NO_x) in the atmosphere, to which traffic is the main contributor, followed by thermal power plants. Other sources include emissions from fires, soils, and lightning.

25 Consequently, NO_x are among the main drivers of air quality degradation in urban areas, and epidemiological studies have shown that nitrogen dioxide (NO₂) exposure is often associated with adverse health effects such as lung cancer, asthma, and cardiopulmonary mortality (e.g., Hamra et al., 2015; Achakulwisut et al., 2019). Therefore, NO₂ is carefully monitored using both surface and satellite instruments, and is often used as an indicator of air pollution. Moreover, NO_x are precursors to secondary aerosols and catalyze the formation of tropospheric ozone (O₃), with consequences for the climate. Due to its short

30 lifetime on the order of a few hours, NO₂ is an excellent marker for anthropogenic emissions, and satellites often show

enhanced NO₂ around large cities and thermal power plants (e.g., Beirle et al., 2003). Therefore, in the past, satellite NO₂ observations have been exploited to evaluate the effectiveness of long-term abatement strategies, the effects of economic recessions, and the impacts of short-term emissions regulations on air quality (e.g., Russell et al., 2012; Lee et al., 2021; Vohra et al., 2022).

35 Along with volatile organic compounds (VOCs), NO_x are major O₃ precursors. Nevertheless, in contrast to rural sites where NO_x-limited conditions usually prevail, in urban locations, under VOC-limited (i.e., NO_x-saturated) conditions, a reduction in NO_x is often associated with an increase in O₃ due to reduction of the NO titration effect (Murphy et al., 2007). Indeed, in recent years, satellite observations showed that, although NO_x emissions are still rising in various developing countries (e.g., India), they have significantly decreased in the majority of the developed countries of North America, Europe, and East Asia
40 (Russell et al., 2012; Geddes et al., 2016; Georgoulas et al., 2019), while tropospheric ozone has increased (Ziemke et al., 2019; Li et al., 2019; Lee et al., 2021). This general tendency has been confirmed in Japan (e.g., Akimoto, 2017) and, recently, in the Kanto region, where both NO₂ and formaldehyde (HCHO) (as a proxy for non-methane VOC, NMVOC) were reduced and O₃ recovered slightly during the period of 2013–2019 (Irie et al., 2021).

Due to their association with human activities, anthropogenic NO_x emissions often display a weekly cycle. The term
45 ‘weekend effect’ refers to the difference in pollutant concentrations between weekdays and weekends (e.g., Cleveland et al., 1974). In the same manner, emissions usually decrease during holiday periods, and an equivalent ‘holiday effect’ can be defined (e.g., Tan et al., 2009). Reduced NO_x levels on rest days are often coupled with increased O₃ in and around cities (Cleveland et al., 1974; Murphy et al., 2007) but not in rural areas (Sicard et al., 2020a). The weekly cycles of both NO₂ and O₃ have been extensively investigated in previous research using both ground-level (Cleveland et al., 1974; Sadanaga et al.,
50 2012; Zou et al., 2019; Sicard et al., 2020a) and satellite (Beirle et al., 2003; Stavrou et al., 2020) observations. A satellite-based analysis of the global temporal evolution of the NO₂ weekly cycle showed that it has become smaller in recent years (Stavrou et al., 2020). This trend has been explained by the current reduction in NO_x emissions, confounding of anthropogenic and background NO_x, and secondarily, by an increase in NO₂ lifetime. On the other hand, a recent study of the O₃ weekend effect revealed a significant downward trend (Sicard et al., 2020a). Overall, analysis of the response of O₃
55 formation to emission changes supports the development of strategies to reduce precursor emissions and improve air quality.

The lockdowns caused by the coronavirus disease 2019 (COVID-19) pandemic represent an opportunity to assess the impacts of human activities on the environment and human health (Gkatzelis et al., 2021; Shakil et al., 2020; Laughner et al., 2021). Recently, many studies have shown that NO₂ levels in 2020 were lower than in previous years due to reduced
60 anthropogenic emissions associated with reduced mobility during temporary lockdowns (e.g., Bauwens et al., 2020; Zander et al., 2020; Cooper et al., 2022). Moreover, these NO₂ reductions in 2020 were associated with surface O₃ enhancement (Sicard et al., 2020b) and reduced O₃ levels in the free troposphere (Steinbrecht et al., 2021; Miyazaki et al., 2021).
Increases in surface O₃ in some cities were explained by a reduction of the NO titration effect (Sicard et al., 2020b).

Deleted: Surface increases in O₃

Formatted: Not Superscript/ Subscript

65 After the first COVID-19 cases in Wuhan, to prevent the spread of the pandemic, strong social distancing and quarantine measures were implemented in many Chinese cities as early as 24 January 2020 till about 25 February; then, measures gradually downgraded to a partial lockdown. Evident decreases in most air pollutant concentrations have been reported for China, with satellite-based NO₂ reductions of about 40 % (Bauwens et al., 2020; Le et al., 2020). In February, TROPOMI NO₂ and HCHO decreased to about 83% and 11% in Wuhan, respectively (Ghahremanloo et al., 2021). Moreover, surface

70 observations showed a general increase in surface ozone in most of the regions, although ozone decreased in the subtropical south and, besides the reduced emissions, meteorological changes were found to be important contributors (Sicard et al., 2020b; Le et al., 2020; Liu et al., 2021). In Korea, the most significant changes occurred in March, with a reduction of about 20% in NO₂ and 45% in PM_{2.5} nationwide, while surface ozone, in contrast with China, was slightly decreased (Ju et al., 2021).

75 Overall, data from various sources suggest a decline in worldwide mobility in 2020 (Nouvellet et al., 2021). Figure 1 shows the change in mobility (amount of people transiting public stations, derived from Google), compared to the pre-COVID period, for some large metropolitan areas around the world deeply affected by the pandemic (further details in Section 2.1.7). The larger reductions (with peaks over 90%) generally coincided with lockdowns, which occurred at slightly different times in different countries. Outside of lockdowns, mobility remained markedly decreased throughout 2020.

80 In Japan, the change in mobility was smaller and more gradual compared to other countries due to the avoidance of strict legal restrictions. However, on February 3, Japan began addressing the issue of the Diamond Princess cruise ship quarantine and on March 3, primary and secondary schools were closed and replaced with remote learning (Table 1). Then, an official state of emergency, when the most stringent restrictions were in effect, was declared from April 7 to May 25. Thereafter, the situation never returned to normal, as new periods of reduced mobility coincided with the second wave of coronavirus

85 infections, which peaked in July–September, and the third wave starting in December.

Table 1. Milestones of the COVID-19 pandemic in Japan.

Date	Milestone
Jan. 15, 2020	First COVID-19 infection
Feb. 3, 2020	Diamond Princess cruise ship quarantine
Feb. 13, 2020	First COVID-19 death
Mar. 3, 2020	Closure of schools
Mar. 11, 2020	COVID-19 declared pandemic by WHO
Mar. 24, 2020	Tokyo Olympic Games postponed
Apr. 7 to May 25, 2020	State of emergency
Jul. 22, 2020	Start of “Go To Travel” program

Jan. 7 to Mar. 7, 2021	State of emergency
Feb. 17, 2021	Start of COVID-19 vaccinations
Jul. 12 to Sep. 30, 2021	State of emergency
Jul. 23 to Aug. 8, 2021	Tokyo 2020 Olympic Games
Aug. 24 to Sep. 5, 2021	Tokyo 2020 Paralympic Games

90 Generally, the mean reduction in mobility was similar among all weekdays and slightly smaller during the weekend in most of the examined countries (Fig. 1b). In contrast to this worldwide trend, Japan showed the largest mobility drop during the weekend, with decreases about 10% larger than on weekdays. Although limited to the state of emergency period and the Tokyo area, this behavior has been observed from other data sources (e.g., Figure 2 in Sugawara et al., 2021) and appears to be a robust feature representing common Japanese habits modified by the spread of the pandemic.

95 Due to this anomalous change in mobility, we suggest that the (relative) NO₂ weekend effect in 2020, primarily driven by traffic, may show peculiar characteristics in Japan. Potentially, this effect could be larger than usual, despite reduced NO_x emissions tending to reduce the anthropogenic weekly signature (Stavrakou et al., 2020). This unique situation provides the opportunity to examine the changes in the air quality that occurred in 2020 in Japan and compare them with previous years. As detailed above, many previous studies examined COVID-related changes in air quality on a global to local scale.

100 Nevertheless, due to somewhat soft countermeasures to limit the spread of the pandemic adopted in Japan with consequent more limited change in the mobility compared with other countries, relatively fewer studies focused on this area (e.g., Itahashi et al., 2022). In some cases, changes in relevant air-quality parameters observed by ground-based or satellite instruments in the Tokyo center during the emergency period have been examined on a local scale (Sugawara et al., 2021) or related to other cities/countries on a global scale (e.g., Cooper et al., 2022) within studies aimed at comparing such

105 variabilities with mobility changes. Nevertheless, as we will see, such changes hide a sizeable spatiotemporal variability and a widespread adherence to recommendations designed to limit the spread of the pandemic, which caused modification of common habits. Those resulted in a unique air quality signature not limited only to the emergency period, which should be examined on a regional scale.

We focused our study on the Greater Tokyo Area (GTA), in the Kanto region, which is the largest area of flat land in Japan, extending inland from the Pacific coast (Fig. 2). It is the most populous metropolitan area in the world and the most important economic hub of East Asia, and local emissions dominate it. Most of this large urban area is expected to be under VOC-limited conditions (Akimoto, 2017; Irie et al., 2021). Nevertheless, western Japan and, to a lesser extent, this region are usually affected by transboundary air pollution from the continent (Itahashi et al., 2022). Due to the strict mobility restrictions implemented in China, this additional contribution is expected to be reduced in early 2020 (Itahashi et al., 2022). This makes the

115 analysis of the COVID-related effects even more complex and points to the necessity of a regional study focusing on
spatiotemporal variability.

In this study, we apply an integrated approach that exploits various independent datasets retrieved from multiple platforms,
including observations of NO₂, O₃, and HCHO (as a proxy for non-methane VOC, NMVOC, Sillman, 1995) from two sites
equipped with Multi-Axis Differential Optical Absorption Spectroscopy (MAX-DOAS) systems located in urban and
120 suburban areas. Further, anthropogenic light-absorbing aerosol data are presented. In contrast to most previous studies,
which have focused on in situ and satellite-based data, observations representative of the boundary layer (< 1 km) provide
our reference data to link surface and satellite column observations.

2 Datasets and methods

2.1 Datasets

125 2.1.1 MAX-DOAS

We used MAX-DOAS observations operated at Chiba University (in 2013-2020) and Tsukuba (in 2015-2020) sites, which
are located in urban and semi-urban environments within the Kanto region (Fig. 2). The MAX-DOAS technique is based on
the well-established DOAS technique (Platt and Stutz, 2008), which utilizes differential absorption structures of trace gases
in ultraviolet (UV) and visible (VIS) wavelength regions to derive aerosol and trace gas information (Hönninger et al.,
130 2004). Our MAX-DOAS system is equipped with a UV-VIS spectrometer located indoors, while an outdoor telescope unit
collects scattered sunlight at reference and off-axis elevation angles. A set of scattered sunlight spectra was measured in a
15-min interval. High-resolution spectra were recorded from 310 to 515 nm using the Maya2000Pro spectrometer (Ocean
Insight, Inc., Orlando, FL, USA) with a slit of 25 μm and a full width at half maximum of approximately 0.3–0.4 nm,
embedded in a temperature-controlled box. Wavelength calibration was performed daily, using a high-resolution solar
135 spectrum, to account for potential long-term degradation of the spectrometer. Retrieval was conducted based on DOAS and
optimal estimation methods using the Japanese MAX-DOAS profile retrieval algorithm, version 2 (JM2) (Irie et al., 2011,
2015) for the following purposes: DOAS fitting, retrieval of the aerosol profile and retrieval of trace gases. In this study,
partial vertical columns of O₃, NO₂, and HCHO concentrations below 1 km were used. Notably, due to the contribution of
upper troposphere/lower stratosphere (UT/LS) O₃ to differential slant column densities, only data collected at a solar zenith
140 angle (SZA) below 50° can be used for O₃ retrieval (Irie et al. 2011, 2021). Therefore, the ozone dataset employed here was
limited to the period of March–October. For cloud screening, measurements with retrieved aerosol optical depth (AOD)
greater than 3 and relative humidity over water greater than 90% were excluded (Takashima et al., 2009). The uncertainty in
the retrieved profiles was further reduced by averaging the data from four collocated MAX-DOAS instruments pointing in
four different directions at the Chiba site (see inset in Fig. 2). This procedure is expected to better account for the potential
145 spatial heterogeneity of tropospheric gases. By contrast, observations from a single MAX-DOAS system were used for the
Tsukuba site. The MAX-DOAS horizontal viewing distance depends on atmospheric conditions (i.e., aerosol load), and can

be up to 24 km in the lowest 1-km vertical layer. Therefore, the MAX-DOAS partial column observations at Chiba are representative of the boundary layer across a region larger than (or comparable to) a usual satellite pixel, but sampled at higher accuracy. Within this framework, it is worth to highlight that our MAX-DOAS observations contributed to recent efforts of the scientific community to validate TROPOMI NO₂ and HCHO datasets at a global scale (Verhoelst et al., 2021; De Smedt et al., 2021).

2.1.2 TROPOMI

The Tropospheric Monitoring Instrument (TROPOMI) onboard the European Union Copernicus Sentinel 5 Precursor (S5P) satellite has a Sun-synchronous orbit with a daily equator crossing time of approximately 13:30 local solar time and daily global coverage (van Geffen et al., 2021). The pixel size of TROPOMI was initially $3.5 \times 7 \text{ km}^2$ and was reduced to $3.5 \times 5.6 \text{ km}^2$ (August 2019), while the swath width is 2,600 km. The imaging spectrometer of this instrument measures radiation in the UV, VIS, near infrared, and shortwave infrared spectral regions (De Smedt et al. 2021; Veeffkind et al., 2012). Operational level 2 (L2) products retrieved from TROPOMI observations include vertical columns of O₃, NO₂, HCHO, carbon monoxide (CO), sulfur dioxide (SO₂), and methane (CH₄). In the following analysis, we used the official TROPOMI NO₂ and HCHO products from the Tropospheric Emission Monitoring Internet Service and the Copernicus Open Access Hub, respectively, recorded between January 2019 and December 2020. The datasets were binned and averaged over a regular grid of $0.1 \times 0.1^\circ$ to perform various statistical analyses at each location (i.e., grid box).

The TM5-MP-DOMINO NO₂ data used in this study are based on the DOMINO retrieval (van Geffen et al., 2019), previously used for Ozone Monitoring Instrument (OMI) data, and exploit the 405–465 nm spectral range to render tropospheric vertical column density with precision of 30–40%. The profile shape of the TM5-MP model is used for computation of the air mass factor (AMF) without accounting for aerosols. Screening of TROPOMI NO₂ data involved retaining data with a quality flag (QF) value higher than 0.5 and a cloud fraction (CF) lower than 0.2. The TM5-MP-DOMINO NO₂ dataset combines the versions 1.2.x. and 1.3.x. Version 1.3.x. was introduced on 2019/02/06, so, essentially, it covers the entire period here examined. Minor differences exist between the versions 1.2.x. and 1.3.x. and, according to all past studies, we combined them (Van Geffen et al., 2021). These differences were caused by improvements in the FRESCO-S algorithm devoted to retrieving cloud information. Indeed, since version 1.3.x., to avoid non-physical cloud fraction and pressure values, when the top of atmosphere reflectance is lower than expected, the surface albedo is reduced to match the top-of-atmosphere reflectance (Van Geffen et al., 2021). A further change in FRESCO is the treatment of very high cloud fractions (Van Geffen et al., 2021). Nevertheless, we excluded observations retrieved under these conditions.

A retrieval algorithm developed for OMI QA4ECV products is used to retrieve TROPOMI L2 HCHO vertical column densities. HCHO slant column densities are retrieved in the 328.5–359 nm fitting window. The HCHO vertical columns are calculated from the retrieved slant column densities and AMF, which is based on TM5-MP. TROPOMI L2 cloud products provide cloud information for AMF calculations. A more explicit explanation of the TROPOMI HCHO retrievals and their validation is provided in the works of De Smedt et al. (2018, 2021). Data filtering was performed as detailed in the product

Formatted: Font: 10 pt, Font color: Auto

180 read-me file (<http://www.tropomi.eu/sites/default/files/files/publicSentinel-5P-Formaldehyde-Readme.pdf>). The current TROPOMI HCHO product is based on version 2.1.3 after 2020/07/13 and version 1.1.x for the period before (De Smedt et al., 2021). The version 2.1.3 includes various improvements compared to the previous version 1.1.x., such as a new surface albedo retrieval algorithm, the adoption of new OCRA cloud-free maps, and the correction of some QF values over snow/ice regions (the latter did not affect the investigated area). More information can be found in the product read-me file and recent validation activities (De Smedt et al., 2021).

Deleted: v

Deleted: v

Formatted: Font color: Auto

2.1.3 OMI

OMI is onboard the National Aeronautics and Space Administration (NASA) Aura satellite, which has a Sun-synchronous polar orbit. OMI passes the Equator around 13:40 LT (local time) and the size of its pixels is 13 km × 24 km at nadir.

We used OMI NO₂ Level-2 data (over Chiba University and Tsukuba sites) and the recently updated Level-3 daily global gridded (0.25 × 0.25°) OMNO2d data V4. The algorithm includes improved surface and cloud treatments (Lamsal et al., 2021). In the following analysis, we exploited observations recorded in 2005–2020, and screened out NO₂ data associated with a cloud fraction larger than 0.3. OMI and TROPOMI NO₂ datasets are based on slightly different retrieval algorithms, including cloud algorithms to estimate cloud fraction. Moreover, the size of the field of view of OMI is larger than that of TROPOMI, and OMI is affected by the row anomaly problem (<http://omi.fmi.fi/anomaly.html>), which further reduces the number of available observations. Here, the slightly larger cloud fraction threshold for OMI than that of TROPOMI tends to counteract the smaller number of available OMI observations (by adding a further 10% of data. More information on the variation of OMI NO₂ as a result of modifying screening criteria can be found in Comperolle et al. (2020)). Since OMI O₃ only has some low sensitivity to the boundary layer while TROPOMI O₃ is currently limited to tropical latitudes, we did not use satellite-based O₃ datasets in this study.

Deleted: 30%

Deleted: potentially

Formatted: Font: 10 pt, Font color: Auto

Formatted: Font: 10 pt, Font color: Auto, Subscript

Formatted: Font: 10 pt, Font color: Auto

Formatted: Font: 10 pt, Font color: Auto

Formatted: Font: 10 pt, Font color: Auto, Subscript

Formatted: Font: 10 pt, Font color: Auto

Formatted: Font: 10 pt, Font color: Auto, Subscript

Formatted: Font: 10 pt, Font color: Auto

Formatted: Font: 10 pt, Font color: Auto, Subscript

Formatted: Font: 10 pt, Font color: Auto

Formatted: Font: 10 pt, Font color: Auto

200 2.1.4 Surface in situ and additional ground observations

In Japan, continuous monitoring of NO_x and other compounds through a capillary surface network is performed by the Atmospheric Environmental Regional Observation System (AEROS). Historical time-series data are accessible to the public via the geographic information system (GIS) of the National Institute for Environmental Studies (NIES) (<http://www.nies.go.jp/igreen/index.html>). As the most recent years are unavailable from the NIES catalog, we limited our analysis to NO₂ observations in 2015–2018. We used a total of 266 stations, including general atmosphere measurement stations and automobile exhaust gas measurement stations in Tokyo, Chiba and Ibaraki prefectures. The measurement principles of O₃, NO_x, and non-methane hydrocarbons are based on UV absorption, NO-O₃ chemiluminescence, and flame ionization detection, respectively.

In addition to the NIES dataset, we used observations of black carbon (BC) concentrations recorded by the continuous soot-monitoring system (COSMOS) (Kondo et al., 2009; Damiani et al., 2021) deployed at Chiba University site in November 2019. Our analysis focused on observations recorded in 2020.

Finally, we combined optical property information retrieved by a sky radiometer with MAX-DOAS data to estimate light-absorbing aerosols within the boundary layer (Damiani et al., 2021), as described in Section 2.2.

2.1.5 CLASS model

220 Simulations with a box model accounting for boundary layer dynamics and chemistry were performed using the Chemistry
Land-surface Atmosphere Soil Slab (CLASS) model (van Stratum et al., 2012; Vilà-Guerau de Arellano et al., 2015). In
these simulations, we used fixed dynamic (i.e., the usual boundary layer height recorded by the collocated lidar instrument)
and chemistry conditions (as in van Stratum et al., 2012), along with the concentrations of NO₂ and HCHO recorded by the
MAX-DOAS system within the boundary layer (at altitudes lower than 1 km) as initial conditions. The model solves the
diurnal evolution of dynamical and chemical species over time in a well-mixed convective planetary boundary layer (PBL)
225 (Vilà-Guerau de Arellano et al., 2015). Since these variables are assumed to be constant with height, the model output
approximates MAX-DOAS observations in the PBL. Chemistry is represented by an O_x-NO_x-VOC-HO_x photochemistry
scheme based on 28 reactions that control O₃ formation. Although this simplified scheme omits other important organic
species and aerosols, CLASS has been shown to reproduce the observed diurnal variability and mixing ratios of the main
reactants present in polluted environments (Zara et al., 2021 and references therein).

230 2.1.6 Copernicus Atmosphere Monitoring Service (CAMS) global reanalysis

CAMS global reanalysis (EAC4) is the latest global reanalysis dataset of atmospheric composition produced by the
European Centre for Medium-Range Weather Forecasts (ECMWF), including aerosols, chemical species and greenhouse
gases (Inneset al., 2019). Atmospheric data are interpolated to 25 pressure levels (top level, 0.1 hPa) at a spatial resolution
of 0.7 × 0.7°. Notably, both OMI (overpass around 13:40 LT) and GOME-2 (overpass around 10 LT) NO₂ data are
235 assimilated in CAMS, but anomalous emissions that occurred in 2020 are not included i.e., the simulations are based on a
business-as-usual emissions scenario. Instead, CAMS uses MACCity anthropogenic emissions and the CO emissions
upgrade described by Stein et al. (2014). Monthly mean VOC emissions were calculated using the MEGAN model.

2.1.7 Additional datasets

Ozonesonde observations were launched from the Tateno Aerological Observatory (Tsukuba, Japan) by the Japan
240 Meteorological Agency (JMA), usually at 3 pm (i.e., around the anticipated time indicating maximum ozone). The KC
ozonesonde used until November 2009 was replaced with an ECC ozonesonde in December 2009. In some of the following
analyses, to fill the gap of the absence of MAX-DOAS O₃ observations in winter (see Sect. 2.1.1), we used data recorded in
the period of 2013–2020 for consistency with the MAX-DOAS time series.

245 MERRA-2 is NASA's latest reanalysis and includes online aerosol fields that interact with model radiation fields (Buchard
et al., 2017; Randles et al., 2017). This product is based on coupling of the Goddard Earth Observing System, Version 5

Earth system model with the Goddard Chemistry Aerosol Radiation and Transport aerosol model. The resolution is 0.625 x 0.5 degree with 72 vertical layers from the surface to approximately 80 km. In the following analysis, we employed data for wind speed, temperature, and PBL height (PBLH).

250 Following previous studies (e.g., Guevara et al., 2021), we used Google mobility data as a proxy for traffic counts as they are easily accessible for the majority of the countries and allowed us to compare the changes that occurred in different regions. Google Mobility data show changes to visits to various places worldwide (<https://www.google.com/covid19/mobility/>). Visits on each day are compared to baseline values for that day of the week. The baseline is the median value for the corresponding day of the week during the 5-week period of Jan 3–Feb 6, 2020. The following place categories are available:

255 Grocery & pharmacy, Parks, Transit stations, Retail & recreation, Residential, and Workplaces. Here, we focused on changes in the Transit stations category (Fig. 1) in certain large metropolitan areas of the world deeply affected by the pandemic. Google transit data has been previously used to estimate the emission reduction for the road transport sector (Guevara et al., 2021). It assumes that mobility trends in public transport hubs can be taken as a proxy for trends in road traffic emissions. This assumption is likely more appropriate for lighter vehicles than for heavier vehicles (Brancher, 2021).

260 2.2 Methods

Except where otherwise noted, we focus on ground-based daily observations recorded between 9 am and 3 pm LT. Weekly changes in NO₂, HCHO, O₃, and light-absorbing aerosols are reported as differences with respect the average value on weekdays. As the strongest reduction of anthropogenic emissions occurs on Sunday in the investigated region, we refer to weekly changes as the difference between the Sunday value and the average of the weekdays. The holiday effect was

265 estimated to be the difference between the average concentration of a given compound during the given holiday period and that in the two 10-day periods immediately before and after the holiday.

Light-absorbing aerosols within the boundary layer were estimated by combining sky radiometer and MAX-DOAS optical property data at UV wavelengths (Damiani et al., 2021). Then, in the following analysis, we examine the fine-mode absorbing AOD within the partial column below 1 km (i.e., fAAOD [0–1 km]), which was computed by combining the

270 columnar fine-mode fraction (FMF) and single scattering albedo (SSA) parameters retrieved from the sky radiometer with the mean partial column AOD estimated from MAX-DOAS measurements. As mineral dust can be strongly absorbing in the UV spectral range, we further removed days with Angstrom exponent (AE) < 1.

Under days characterized by stagnant low wind speed conditions, NO₂ accumulates around source locations. In contrast, under days with high wind speed conditions, NO₂ is dispersed. Tokyo is located in a polluted background with various

275 significant NO_x sources surrounding it within about a 100 km radius. Therefore, due to the influence of surrounding sources, the outflow plume of NO₂ from Tokyo is not evident in the TROPOMI NO₂ maps. However, the spatial pattern of the difference between these two NO₂ composites, built based on wind speed data, reveals outflow patterns more clearly (see also Liu et al., 2016). We applied this method limitedly to Fig. 5c. To select the threshold values to identify high and low wind speed days for each pixel, we used MERRA-2 wind fields. According to previous studies (e.g., Fioletov et al., 2022), we

280 used a PBL averaged wind. Still, the results are not sensitive to the wind altitude because the wind is relatively constant
within the boundary layer. Composite differences between high and low wind speed days in TROPOMI NO₂ were computed
based on MERRA-2 wind fields averaged around the overpass time (12–3 pm). The median wind speed of each pixel was
assumed to be the threshold between the high and low wind values. We first regridded the MERRA-2 data to the resolution
of TROPOMI; then, for each grid cell, we computed NO₂ as the difference between the composite values of days with high
285 and low wind speed.

3 Results

3.1 Trends and seasonal changes

The spatial distribution of the TROPOMI NO₂ and HCHO column data in the Kanto region is shown in Fig. 3 for 2019 and
2020 on an annual basis (top panels) and during the state of emergency (bottom panels). The bulk of NO₂ is around Tokyo,
290 which is the most densely populated area (Fig. 2), including along the main transportation routes, and extends toward the
south, where various large power plants and industrial activities are located (left column in Fig. 3). Overall, on an annual
basis, column NO₂ over the GTA was reduced by about 10% in 2020 compared to 2019 (Fig. 3m), with larger absolute
reductions around Haneda and Narita international airports, while smaller changes occurred in areas characterized by the
presence of multiple power plants (South of Chiba). On the other hand, during the state of emergency, TROPOMI shows the
295 largest NO₂ reduction (20–40%) in the southern Tokyo area while limited reductions (about 10%) occurred around Chiba
and Tsukuba (Fig. 3o). The area affected by the most significant NO₂ reduction coincides with the region characterized by
the larger decrease in traffic counts (Takane et al., 2022). Assuming that traffic currently contributes about 40% of Japanese
domestic NO_x emissions (Kurokawa and Ohara, 2020), a drop in mobility by about 50% in April–May (Fig. 1) is consistent
with the TROPOMI-based estimate of NO₂ changes related to COVID.

300 Aside from anthropogenic emissions, meteorological conditions contribute to determining the interannual variability of NO₂.
Annual differences between 2020 and 2019 in major meteorological parameters such as wind speed, surface temperature and
PBLH, which are expected to influence the NO₂ distribution, were quite limited (Fig. S1a–c). In contrast, during the state of
emergency, the wind speed in 2020 was slightly higher than that of 2019 and potentially contributed to further reducing the
NO₂ levels (Fig. S1d).

305 Based on satellite observations and model simulations, Cooper et al. (2022) estimated a significant overall decrease in
surface NO₂ over more than 200 cities around the world in April 2020 compared with 2019. Among others, they reported
NO₂ changes for various Japanese cities. Within the Kanto region, they showed reductions peaking at Yokohama (-69%),
more minor changes at Saitama (-32%), and values roughly in between at Tokyo (-54%). Despite the inverse correlation
between the lockdown Stringency Index and the NO₂, they found that changes in Japan were comparable or slightly lower
310 than those for the European cities where lockdown restrictions were much more stringent. In agreement with our findings
(Fig. S1d and Fig. S3), they showed that changes in Japan could have been favored by meteorology and long NO₂ trends.

Although the period examined by Cooper et al. (2022) only partially coincides with the Japanese state of emergency, Fig. 3o shows comparable reductions. Moreover, Fig. 3o reveals the complex pattern of these variations, characterized by an evident North-South gradient with the most significant (negative) changes in Southern Tokyo, further evolving toward zero changes
315 in the Saitama prefecture. This highlights the necessity of coupling detailed analysis at a regional scale with a large-scale study when examining COVID-related impacts, particularly when focusing on areas dominated by several close megacities.

Despite the high spatial heterogeneity of HCHO concentrations due to its short lifetime, the spatial distribution of the TROPOMI HCHO column was estimated (Panel (e-h) in Fig. 3). While NO₂ variability is dominated by anthropogenic activities, HCHO arises from both anthropogenic and natural sources. The principal source of HCHO is the oxidation of
320 methane, which provides a global ambient background (e.g., Surl et al., 2018). Then, over continental atmospheres, the main anthropogenic sources are vehicle exhaust emissions and industrial emissions, while the main natural sources are plants and biomass burning (Surl et al., 2018; Sun et al. 2021; Ghahremanloo et al., 2021). Although the general increasing gradient from the ocean toward the continent resembles the pattern of NO₂, the HCHO distribution is not well defined and does not align with the urbanized region. The somewhat higher HCHO concentration in 2020 (Fig. 3n), despite lower anthropogenic
325 emissions, may be driven by small differences in temperature between the two years (Fig. S1b). However, the change in meteorological conditions and the application of cloud screening cause the amount of data collected under clear sky conditions to be slightly different each year. Then, also the distribution along the year of the data can be different. For example, due to the rise in the summertime HCHO concentration, if frequent clouds caused few TROPOMI observations collected in the summer of a given year, the mean annual concentration of such a year could be smaller than the mean of the
330 other year characterized by more summer HCHO observations. This confounding factor complicated the interpretation of HCHO changes. Then, despite the lower temperature that occurred during the state of emergency (Fig. S1e), TROPOMI did not show evident differences in the HCHO pattern between the two years (Fig. 3p).

A summer maximum characterizes the observed seasonal cycle of the HCHO columns shown in Fig. 4g. This indicates that biogenic emissions dominate HCHO even within our urban region. Pieces of evidence in TROPOMI HCHO reductions as a
335 consequence of the COVID-related mobility restrictions have been reported only for China (Ghahremanloo et al., 2021) while meteorology likely drove most of the HCHO variations in India (Levelt et al., 2022). However, even in Wuhan, while the reduction in NO₂ reached about 83%, the decrease in HCHO was only 11%. The recent study by Sun et al. (2021) showed that comparable HCHO reductions (i.e., 11%) were found in the Northern China Plain for locations with predominant declines in NO₂ columns and elevated anthropogenic NMVOC emissions. However, reductions were favored
340 by meteorological conditions. Then, simulations showed that most of the HCHO decrease resulted from the reduced anthropogenic NO_x emissions. Still, an additional reduction in anthropogenic NMVOC emissions of about 15% would be necessary to match the observations (Sun et al., 2021). Since mobility restrictions in Japan were less severe and more gradual than those established in China, we expect such minor HCHO variations hardly identifiable by using satellite observations.

The HCHO-to-NO₂ concentration ratio is an indicator of near-surface O₃ sensitivity (e.g., Martin et al. 2004). Traditionally,
345 the ozone production regime is considered to be VOC-limited when this ratio is lower than 1, NO_x-limited when it is higher

than 2, while ozone is expected to be in the transition regime when the values are in the range 1–2 (Duncan et al., 2010; Ryan et al., 2020). Although several studies used this ratio to infer O₃ sensitivity to NO_x and VOCs by using observations from satellite and ground-based instruments (Duncan et al., 2010; Jin et al., 2017; Schroeder et al., 2017; Irie et al., 2021), some limitations still exist. Assuming the transition region lies within the range 1–2 (Duncan et al., 2010) could not be valid at global levels, and it could be necessary to compute it depending on the region (Schroeder et al., 2017). Moreover, the ratio has an altitude dependence (e.g., Jin et al., 2017; Schroeder et al., 2017). While seasonal variations and trends in the columnar HCHO/NO₂ ratio (i.e., based on satellite observations) generally match the ratio computed with in situ observations, magnitudes are often different due to different vertical distributions of HCHO and NO₂ (Ryan et al., 2020). Therefore, although O₃ sensitivity derived from satellite column data can differ somewhat from that based on in situ observations (Schroeder et al. 2017), it nonetheless provides useful information and has been extensively studied in relation to COVID-19 (e.g., Ghahremanloo et al., 2021 among others). The HCHO/NO₂ ratios are shown in Fig. 3i–l. Overall, the ratio increased in 2020, indicating a shift toward more NO_x-limited conditions. This change is particularly evident for Tsukuba, where the ratio rose from 2.1 to 2.9, while limited variations occurred over Tokyo and Chiba. We can observe similar findings during the emergency period (Fig. 3k,l).

To further contextualize the changes that occurred in 2020, Fig. 4 shows monthly partial column NO₂, O₃, HCHO, as well as light-absorbing aerosols within the boundary layer (i.e., < 1 km) recorded at Chiba University. To better account for the spatial heterogeneity of tropospheric gases, the average values from four MAX-DOAS systems looking at different directions were employed (Section 2.1.1 and Fig. 2). As shown in a recent study (Irie et al., 2021), both NO₂ and HCHO were reduced and O₃ increased slightly during the period of 2013–2019. Any potential COVID-related effects in 2020 were superimposed over these trends. Indeed, in 2020, NO₂ remained at its lowest recorded levels for almost the entire year, whereas HCHO was only occasionally lower in 2020 than 2019, particularly in the second half of the year, and no modulation of O₃ was evident. When analysis was limited to the period of the state of emergency (i.e., roughly April–May), all species considered here showed decreases in May compared with the same period of 2019 while some enhancements in April. This is coherent with an electricity demand reduction in May more significant than April for Chiba and the other Prefectures of the Kanto region (data from the Japanese Agency for Natural Resources and Energy available at https://www.enecho.meti.go.jp/statistics/electric_power/ep002/results_archive.html).

Overall, in agreement with the tropospheric column observations (Fig. 3o,p), slight changes occurred in the boundary layer around Chiba during the emergency period. In addition to the decrease in NO₂, similar month-to-month variabilities in HCHO and O₃ are apparent from the differences between 2020 and 2019.

Miyazaki et al. (2021) showed that the pandemic caused a reduction in global NO_x emissions which resulted in an overall decreased free-tropospheric ozone and some isolated enhancements, due to titration effect, at the surface in correspondence with some strongly urbanized regions (mostly in China). Although they mostly focused on a global scale, so their study is hardly comparable with our findings at regional scale, this expected opposite change of ozone with the altitude suggests that

380 MAX-DOAS ozone could result in negligible changes due to summing up of positive and negative changes within the column.

As a further reference, we compared the observed changes with equivalent CAMS data (Innes et al., 2019), which assimilate satellite observations of tropospheric NO₂ (Section 2.1.6). CAMS data roughly reproduced the observed interannual and seasonal variabilities (Fig. 4). However, while the trends in NO₂ and O₃ were comparable to observations, CAMS did not reproduce the HCHO decrease; instead, an increasing trend was simulated. The month-to-month variability was very similar to that of observations. Nevertheless, the CAMS NO₂ difference between 2020 and 2019 was generally smaller than the observed difference (Fig. 4i). Although satellite NO₂ data are assimilated in CAMS, the impact of assimilation is expected to be limited for short-lived species such as NO₂ (Innes et al., 2019). Therefore, as CAMS simulations did not include the anomalous 2020 emissions, comparison of CAMS and MAX-DOAS datasets supports the possibility that the emissions reduction in 2020 was responsible for the observed stronger NO₂ decrease. On the other hand, CAMS satisfactorily reproduced the month-to-month variabilities of both O₃ and HCHO.

Finally, we considered the changes in light-absorbing aerosol in both the boundary layer and the total column. Although this dataset is characterized by high uncertainty (Damiani et al., 2021), the values in 2020 were clearly the lowest on record. The largest relative changes (not shown) occurred before the state of emergency (i.e., in January and February), while the largest absolute change occurred in fall; nonetheless, some reduction was apparent in May. In this huge urbanized region, light-absorbing aerosols tend to be produced mainly by local pollution. However, transboundary transport has been shown to further modulate the light-absorbing aerosol dataset (Damiani et al., 2021), complicating the attribution of effects to the pandemic.

3.2 Weekend, holiday, and wind effects from various platforms

400 Previous studies (e.g., Beirle et al., 2003) have reported that apparent signatures of anthropogenic activity reflect a weekly cycle of NO₂ over most major cities in the northern hemisphere. To contextualize the weekly changes occurring in the GTA, we analyzed global OMI NO₂ data for the period of 2005–2020. Figure 5a and Table S1 show the global ranking of the resulting relative changes on Sunday over cities with population larger than 0.5 million inhabitants (we implicitly excluded cities where the rest day is on Friday; see Stavrakou et al., 2020). For the sake of clarity, we report only those cities with changes more prominent than 30%, although the majority of locations showed negative values (except in China; Stavrakou et al., 2020). Japanese cities dominate the histogram; worldwide, the extent of changes over the GTA is exceeded only by Los Angeles and São Paulo. The OMI-based map of such changes (Fig. 5b) shows a well-defined pattern over Japan, with consistent values negative across the country, which were lower than –40% over most of the GTA and industrialized regions in southern Japan (i.e., Nagoya, Osaka).

410 Power plants and other industrial facilities are the dominant stationary emissions sources, and are generally consistent, with little effect of weekly modulation. Satellite NO₂ data can be used to investigate both stationary (Beirle et al., 2019) and

mobility-related emissions sources (Ialongo et al., 2020). Using satellite NO₂ and wind field data, emissions related to large and isolated stationary sources can be assessed (Beirle et al., 2019). Nevertheless, when multiple stationary sources are
415 located within an urbanized region, as in our study area, evaluating the impacts of the various sources becomes challenging. As shown in Fig. 5c, we exploited the high resolution of TROPOMI data to compare NO₂ changes associated with the weekly cycle (i.e., Sunday minus weekdays, red contours) to NO₂ changes associated with wind speed (high wind speed days minus low wind speed days, black contours; see Sect 2.2 for further details) in 2019–2020. Moreover, to better highlight the spatial patterns of these changes, we focused on the extended summer period from April to September, when the NO₂
420 lifetime is shorter and NO₂ tracks emissions sources better. Both contour lines suggest larger reductions over Tokyo than other areas, with patterns mostly matching the spatial distribution of population density. The weekly related NO₂ generally extends north to Tsukuba and east to Chiba with a roughly homogeneous spatial gradient, while the gradient sharpens south of Chiba.

During days characterized by stagnant wind conditions, NO₂ levels tend to accumulate around stationary sources, while rapid
425 transport occurs with stronger winds. In addition to covering areas with high population density, high negative wind-related changes are apparent around the main power plants on both sides of Tokyo Bay. Moreover, detailed distributions around stationary sources have been revealed (e.g., changes around Narita international airport and the isolated Kashima power plant on the east coast of Chiba Peninsula). Overall, the distribution of wind-related changes is more southerly than the bulk of weekly changes. Moreover, this gradient becomes positive in the north, highlighting the region downwind of the Tokyo
430 area, including Tsukuba. Overall, wind-related NO₂ changes closely resemble the pattern shown in the Japanese Emission Inventory.

The map in Fig. 5d shows the NO₂ decrease occurring during the end-of-year holiday, when most anthropogenic emissions are reduced. To quantify this holiday effect, the average NO₂ value of the 10 days before and after the holiday (defined here as the period from 25 December to 4 January) was subtracted from the holiday mean. Figure 5d shows similar patterns to
435 Fig. 5b, although the longer NO_x lifetime in winter causes the changes to be less confined to urbanized regions. TROPOMI NO₂ decreased by about –43 and –49% in Chiba and Tsukuba, respectively (Fig. S2). The holiday effect is apparent in almost all cities with intense weekly cycles (Fig. 5a) and will be used as a further reference.

Multi-year MAX-DOAS observations of partial column NO₂ recorded at Chiba University also showed a decrease around the end of the year (Fig. S2). It was about –44%, while smaller changes occurred in HCHO (about –15%). Slightly larger
440 reductions were observed at Tsukuba site (–55% and 29%, for NO₂ and HCHO, respectively).

Focusing on the holiday period provides insights into the response of O₃ to these significant changes. As only data at SZA lower than 50° can be used to retrieve O₃ with the DOAS method (Irie et al. 2011; see Sect. 2), we focused on ozonesonde profiles recorded at the Tateno Observatory, located about 50 km from Chiba. In this manner, we assessed the vertical distribution of O₃ changes within and slightly above the PBL. These data were used to better interpret the changes in partial
445 column O₃ estimated by the MAX-DOAS systems. In the lower troposphere, the average O₃ profile concentration averaged across business days was smaller than the O₃ concentration recorded during the end-of-year holiday (Fig. 5e). The difference

was greatest in the lowest layers (about -18%) and remained nearly constant up to 0.5 km; then, it became smaller and disappeared above 1 km. The reduced NO titration effect occurring under VOC-limited conditions is likely the main driver of this peculiar pattern of increased O₃ levels in the lowest layers during the holiday period.

450 We simulated the periods of 2019 and 2020 with the CLASS model using the appropriate mean NO₂ and HCHO observations and lidar-based PBLH recorded at Chiba as initial conditions. The results of the simulations (vertical lines in Fig. 5e) confirmed the holiday-associated positive O₃ enhancement, with a relative difference of 22% at 15:00 LT, which was also the time of the sonde launch corresponding to the diurnal ozone peak. Previous studies have reported comparable O₃ enhancement effects on the weekend, particularly in winter (Sadanaga et al., 2012; Sicard et al., 2020a). Using the same
455 approach, we evaluated the changes occurring around mid-August, which is a period of reduced mobility. Such changes are interesting in terms of the O₃ formation regime, but significant variability prevented clear identification of trends (Fig. S2).

Figure 6 further characterizes the NO₂ weekend effect and contextualizes the holiday effect through comparison of ground-based partial column (< 1 km), satellite-based tropospheric column, and surface in situ observations. In Chiba, relocation of
460 all four instruments occurred in 2014 (i.e., the pointing direction of some sensors was changed slightly; Irie et al., 2021); therefore, in the following analysis, we excluded observations recorded in 2013 and 2014. Panel (a) shows the geographic distribution of NO₂ weekly changes on Sunday for OMI, with MAX-DOAS and in situ observations plotted together. We focused on 2015–2018, when all three datasets were available. The spatial distribution of OMI NO₂ is as shown in Fig. 5b. The largest negative changes occurred over Tokyo, which reached -45%, and changes became smaller toward Chiba and
465 Tsukuba. Notably, the magnitude of these changes is larger around Tsukuba (-35%) than around Chiba (-30%), although Tsukuba is a suburban site, while the urban area of Chiba hosts a larger population (Fig. 2) and industrial activities. In situ observations match the satellite-based spatial distribution, although with a somewhat smaller magnitude (by about 5%).

MAX-DOAS partial column data reproduced the spatial distribution of the previous datasets (inset in Fig. 6a), showing a magnitude of change slightly closer to that of OMI (i.e., total column) than the surface network. Both in situ and MAX-
470 DOAS observations were averaged over 9 am–3 pm, while OMI observations were generally recorded around 1:30 pm. The small incongruence among measurements is likely due to the different sampling periods (i.e., while in situ observations include data recorded under all meteorological conditions, satellite and MAX-DOAS data were limited to clear-sky days).

We also compared the climatology of the weekly cycle from various platforms according to data availability (excluding 2020). For comparison with the other datasets, we used the mean value from the in situ stations within Chiba (Fig. 6b) and
475 Ibaraki (Fig. 6c) prefectures, respectively. Despite the different periods analyzed, the weekly cycles were very similar for all three platforms. The magnitude of change is largest on Sunday; at Chiba, OMI changes are approximately 10% larger than both ground observation types. By contrast, at Tsukuba, in situ data are lower than OMI and MAX-DOAS by 10–15% (but due to the scarcity of in situ stations around Tsukuba, the average value of stations inside Ibaraki prefecture is likely not representative of the area around Tsukuba). In addition to Sunday, indications of reduced NO₂ are apparent on Friday and
480 Saturday at both sites. As a further reference, we included the NO₂ weekly cycle of Tokyo Prefecture. The data confirmed

that weekly cycles are similar in the three prefectures, with values for Tokyo on Sundays being about 5–10% larger than in other prefectures.

Figure 6d and 6e show changes in OMI NO₂ on Sunday averaged over the periods of 2005–2007, 2015–2019, and 2005–2019 at Chiba and Tsukuba, respectively. The OMI NO₂ column over the investigated region decreased by about 50% over 485 2005–2019 (see Fig. S3 for Chiba). Therefore, in accordance with a previous study (Stavrakou et al., 2020), the weekly cycle showed a reduced amplitude in recent years. During this latest period, in situ, satellite, and MAX-DOAS observations at Chiba coincided, while these data sources showed a spread of about 15% at Tsukuba. This larger variability at Tsukuba is likely due to its lower NO₂ levels and suburban location downwind of the Tokyo area (Fig. 5c).

As a further reference, Fig. 6d,e also show the end-of-year holiday reductions. Overall, when considering the full 2005–2019 490 period, OMI holiday changes were larger than OMI Sunday changes by about 8% for both Chiba and Tsukuba. However, in recent years, NO₂ values were much larger on holidays than on Sundays.

For Chiba, the distinct Sunday changes recorded by each of the four MAX-DOAS instruments were also investigated. The instruments showed a spread of less than 10% with limited interannual variability. The amplitude of the NO₂ weekend effect differed among instruments, with smaller effects for the instruments pointing south and east than for those pointing north and 495 west. This difference was likely due to the presence of power plants and industrial activities within a few tens of km south of the sampling site, providing an additional and more constant emissions source that reduces the difference between rest and business days. Indeed, absolute NO₂ amounts were generally higher for the MAX-DOAS facing south, followed by the east-, west-, and finally north-facing instruments (inset in Fig. S3).

Moreover, changes in MAX-DOAS NO₂ were much more prominent in 2020 than in previous years. Notably, 2020 was 500 equally anomalous for all instruments, with decreases around 15–20%. Therefore, the observed decrease was not a local phenomenon. Generally, MAX-DOAS changes at Tsukuba are more significant than the data recorded at Chiba. Nevertheless, at Tsukuba, changes in 2020 were within the usual level of interannual variability. Therefore, the anomalous weekly cycle in 2020 affected the urban region of Chiba but not suburban area.

3.3 Weekly cycles

505 3.3.1 Weekly cycle of partial column NO₂, HCHO, O₃ and light-absorbing aerosols

Figure 7 shows the interannual weekly changes in MAX-DOAS partial columns of NO₂, HCHO, O₃, and HCHO/NO₂ at Chiba and Tsukuba sites. Further changes in fAAOD [0–1 km] were reported for Chiba only. As we used observations averaged over four independent MAX-DOAS systems at Chiba, the data are more statistically robust and representative of a larger area than observations from Tsukuba (sampled with only one instrument). Therefore, most of the following discussion 510 on interannual changes is focused on Chiba.

As noted above, at Chiba, while the NO₂ change on Sunday was approximately –30% for 2015–2019, it reached about –45% in 2020. This difference was much larger than $2 \times \sigma$ (Fig. S4). On the other hand, except in 2020, interannual variability

was much smaller on Sunday than on other days. By contrast, at Tsukuba, Sunday changes in 2020 were comparable to those in previous years.

515 Usually, the weekend effect was absent in HCHO data from both Chiba and Tsukuba. Nevertheless, at Chiba, negative HCHO changes on Sunday 2020 were unprecedentedly large (around -30%). This negative anomaly is larger than the largest deviation on any other day in previous years, and can be attributed to abnormally low anthropogenic NMVOC on the Sundays of 2020 (Sun et al., 2021; Ghahremanloo et al., 2021). By contrast, HCHO showed no unusual trends at Tsukuba in 2020, and this difference is likely due to differences in local conditions (i.e., Tsukuba is located in a suburban area, where a
520 greater amount of biogenic VOC emissions contribute to HCHO concentrations) and higher variability associated with the usage of only one instrument.

A weekly cycle in the HCHO/NO₂ ratio is evident for Tsukuba, with its peak on Sunday (approximately double the weekday average). On the other hand, for Chiba, the slightly higher ratio on Sunday was similar to the value on weekdays (0.55 vs. 0.4). Notably, on almost all days of 2020, the HCHO/NO₂ ratio at Tsukuba was higher than in previous years, while no
525 difference was recorded at Chiba. Overall, due to the seasonal variations in NO₂ and HCHO concentrations, the HCHO/NO₂ ratio also shows significant seasonality, with a large ratio in summer compared to the other seasons (Irie et al., 2021). Nevertheless, the frequent cloudy conditions in the late-spring to summer period and the limited temporal extension of the dataset prevent to evaluate potential seasonal differences in its weekly cycle.

Despite this large variation in the main precursors, corresponding modulations in the O₃ partial column were not recorded on
530 Sundays of 2020 or previous years. Although the amplitude of the weekend effect in ozone is likely to have been reduced in recent years (Sicard et al., 2020a), its absence in our data contrasts with previous results showing a discernible weekend effect in surface ozone at Tokyo (Sadanaga et al., 2012). Ozone in the free troposphere presents a greatly smoothed diurnal cycle, if any, compared to surface ozone and this diurnal cycle is generally strongest below 950 hPa (Petetin et al., 2016). The ozone profile is different from the other trace gases. In contrast to NO₂, which strongly decreases its concentration with
535 altitude, ozone concentration does not decrease with altitude. The ozone weekend effect at the surface level is usually 10% (Sadanaga et al., 2012) and is much less evident than NO₂. As suggested by ozonesonde observations (Fig. 5e), ozone changes due to titration maximize at the surface and tend to reduce shortly at h > 0.5 km. Since MAX-DOAS O₃ partial column observations sample the 0-1 km layer, the effect tends to disappear in our data. Moreover, more titration is expected in winter, but MAX-DOAS O₃ observations were unavailable this season (Sect. 2.1.1). Finally, the number of MAX-DOAS
540 daily ozone samples was generally smaller than the other trace gases. Therefore, any potential weekly cycle would be difficult to observe in our MAX-DOAS O₃ partial column dataset.

We further evaluated potential ozone differences between Sundays and weekdays of 2015–2020 using the box model (not shown). As in the previous simulations, we used MAX-DOAS observations of NO₂ and HCHO and lidar-based PBLH as initial conditions and focused on the period most strongly affected by the pandemic (i.e., April–September). The simulated
545 ozone differences between Sundays and weekdays were slightly negative (i.e., Sunday O₃ < weekday O₃) and ranged from -4% in 2018 to -8% in 2020.

Formatted: Font: 10 pt, Font color: Auto

Formatted: Font: 10 pt, Font color: Auto, Subscript

Formatted: Font: 10 pt, Font color: Auto

Formatted: Font: 10 pt, Font color: Auto, Subscript

Formatted: Font: 10 pt, Font color: Auto

Formatted: Font: 10 pt, Font color: Auto

As shown in the bottom panel, we examined the weekly cycle of fAAOD partial column data at Chiba. Although such data are characterized by high interannual variability, similar to the results presented above, 2020 data were anomalous, characterized by negative changes of about 50% on Sunday and no variation on Saturday. Notably, consistent with the results for NO₂ (Fig. 6d), changes in fAAOD on Sundays in 2020 are comparable with the effect usually observed during the end-of-year holiday. Although the weekly cycle is hardly discernible in the other years, the weekly cycle in 2020 is coherent with that of collocated observations of surface BC mass concentration, which show reductions larger than 40% on Sunday and no change on Saturday.

We further excluded the influence of meteorology on the observed interannual variation by examining data on wind speed, wind direction, and temperature recorded at Chiba on days with available MAX-DOAS observations (Fig S5). Overall, the results showed that wind did not drive the weekly changes in tropospheric gases. As increasing temperature enhances biogenic emissions and boosts oxidation processes, temperature is usually positively correlated with HCHO. We verified the absence of apparent weekly variation in temperature. Moreover, due to the large amount of data recorded at Chiba site, we could confirm that weekly changes around the satellite overpass time were representative of the daily NO₂. No apparent difference between MAX-DOAS daily NO₂ for 9:00–15:00 and for 12:00–15:00 was observed (the same result was obtained for HCHO and O₃).

3.3.2 Weekly cycle of TROPOMI NO₂ tropospheric columns

Next, we examined the pattern of weekly changes in TROPOMI NO₂, looking for differences in the spatial distribution and magnitude of Sunday changes between 2019 and 2020 (Fig. 8). Overall, changes were larger in 2020 than in 2019, reaching –50% over central Tokyo. Moreover, during the extended summer period (April to September), when the largest influence of COVID is expected, differences between 2020 and 2019 were even more apparent. In addition to the magnitude of the differences, the area characterized by higher NO₂ concentrations was greatly reduced in 2020 compared to 2019. This reduction averaged about –27% for weekdays and reached –67% for Sundays (Fig. S6).

Within the areas sampled by the MAX-DOAS systems, TROPOMI showed no clear differences between 2019 and 2020 in either Chiba or Tsukuba. For Chiba, this contrasts with ground observations. Different time windows, over which the daily means were computed (i.e., between 9 am and 3 pm for MAX-DOAS and around 1.30 pm for TROPOMI), and cloud screening procedures resulted in a larger amount of MAX-DOAS data than satellite data and likely contributed to these differences. However, despite being based on one year of observations, both TROPOMI maps could correctly reproduce the spatial pattern of changes estimated from ground-based observations around Chiba, i.e., the north-south gradient driven by the presence of power plants. This similarity provides confidence in identifying the interannual variability of the spatial distribution of the NO₂ weekly cycle based on TROPOMI data.

4. Discussion and conclusions

580 This study investigated the interannual, seasonal, weekly variabilities and spatial distributions in NO₂, HCHO, O₃, and light-absorbing aerosols measured with multiple platforms within the Greater Tokyo Area, which is the most populous metropolitan area in the world. We mainly examined the period of 2013–2020, focusing on 2020, when an effect from COVID-19 is expected. The main results can be summarized as follows:

- In 2020, levels of NO₂ and light-absorbing aerosols were the lowest on record, but the potential COVID-19 impact was superimposed on a decreasing trend.
585
- At Chiba, MAX-DOAS observations within the PBL showed that annual NO₂ reductions in 2020 were about 10% relative to 2019 with limited changes during the period of the state of emergency. No deviations in O₃ and HCHO were apparent.
- TROPOMI column-based observations confirmed the observed reduction in NO₂ and the absence of relevant changes in HCHO. During the state of emergency, NO₂ reductions exceeded 40% in the southern Tokyo area but were about 10% over Chiba and Tsukuba. Moreover, both satellite and MAX-DOAS observations showed enhancement of the HCHO/NO₂ ratio,
590 which was strongest in the suburban region.
- OMI observations demonstrated that the weekly and holiday effects in NO₂ within the GTA are among the largest in the world. NO₂ reductions on rest days are not limited to the GTA but extend uniformly over most of Japan.
- Surface in situ, MAX-DOAS partial column and satellite-based tropospheric column observations showed a coherent NO₂
595 weekly cycle, with the largest reductions on Sunday. Ground observations aligned with the spatial distribution of the satellite changes, even within the relatively limited area sampled by the MAX-DOAS systems.
- In 2020, ground and satellite observations showed an anomalous weekly cycle in NO₂ in urban areas, with larger reductions on Sunday than in previous years. Similar large changes in light-absorbing aerosols were identified. Such changes are comparable to the reductions observed during the end-of-year holiday period.
- At Chiba, large NO₂ reductions on Sunday were coupled with simultaneous reduction of HCHO, whereas no significant
600 changes in O₃ were observed.
- In Japan, the reduction in mobility in 2020 was more extensive on the weekend than on business days, in accordance with the larger NO₂ weekly change in 2020 found in the urban areas. By contrast, other countries generally showed the opposite behavior. This highlights modification of habits by the Japanese populace that resulted in unique air quality effects,
605 suggesting widespread adoption of recommendations aimed at limiting the spread of the pandemic in Japan despite the lack of strict legal restrictions.

Although not explicitly mentioned in the previous discussion, an implicit assumption of our study relies on the fact that satellite observations available only around midday are representative of daily changes computed, for example, by hourly observations. Although we provide evidence that this is likely the case (see Fig. S5), data from new geostationary satellites
610 (e.g., Geostationary Environment Monitoring Spectrometer on board the Geostationary Korea Multi-Purpose Satellite 2) are expected to shed some further light on this issue.

A further shortcoming is the scarcity of reliable [satellite-based](#) tropospheric ozone datasets to complement the satellite-based spatial distribution achieved with NO₂ and HCHO observations. Despite the recent progress (Shen et al., 2019), OMI O₃ only has some low sensitivity to the boundary layer, and this would make challenging any analysis over the investigated region
615 (past studies found some correlation with the actual surface ozone in China, where tropospheric ozone is much larger, Shen et al., 2019). TROPOMI is expected to improve this capability soon, but its ozone dataset is currently limited to tropical latitudes.

Finally, it is worth mentioning the potential impact of the rebound of the long-range transport of pollutants after the Chinese economic recovery from the COVID-19 pandemic (Itahashi et al., 2022) on the current pollution within the Kanto region
620 will deserve further investigation.

Data availability. All datasets used in the present study are publicly available below:

<https://www.temis.nl/>

<https://scihub.copernicus.eu/>

<https://disc.gsfc.nasa.gov/>

625 <https://woude.org/>

<https://www.google.com/covid19/mobility/>

<http://atmos3.cr.chiba-u.jp/skynet/>

<http://atmos3.cr.chiba-u.jp/a-sky/>

<https://www.ecmwf.int/en/forecasts/dataset/cams-global-reanalysis>

630 <http://www.nies.go.jp/igreen/index.html>

Author contribution. Conceptualization, A.D.; Methodology A.D. and R.C.C.; Measurements and data curation, H.I.; Analysis, A.D., D.B., S.H.H., and S.K.; Funding acquisition: H.I.; Writing—review and editing, A.D., H.I., D.B., R.R.C.; all authors have read and agreed to the published version of the manuscript.

Competing interests. The authors declare that they have no conflict of Interest.

635 **Acknowledgements.** This research was supported by the Environment Research and Technology Development Fund (JPMEERF20192001 and JPMEERF20215005) of the Environmental Restoration and Conservation Agency of Japan, JSPS KAKENHI (grant numbers JP19H04235, JP20H04320, JP22H03727, JP22H05004 and JP21K12227), the JAXA 2nd research announcement on the Earth Observations (grant number 19RT000351) and the Virtual Laboratory (VL) project by the Ministry of Education, Culture, Sports, Science and Technology (MEXT), Japan. [R.R.C. acknowledges the support of the](#)
640 [Consejo Nacional de Ciencias y Tecnología \(CONICYT, Preis ANILLO ACT210046\)](#). The authors would like to thank the OMI and TROPOMI Science Teams for the data products, CAMS and MERRA-2 for the corresponding reanalysis data products, and JMA, AEROS & NIES staff.

Formatted: Font: 10 pt, Font color: Auto

Formatted: Font: (Default) Times New Roman, (Asian) Times New Roman, 10 pt, Font color: Auto

Formatted: Font: 10 pt, Font color: Auto

Formatted: Font: Not Bold, Font color: Auto

References

- 645 Achakulwisut, P., Brauer, M., Hystad, P., Anenberg, S.C.: Global, national, and urban burdens of paediatric asthma incidence attributable to ambient NO₂ pollution: estimates from global datasets, *Lancet Planet Health*, 3, e166–78, DOI:[https://doi.org/10.1016/S2542-5196\(19\)30046-4](https://doi.org/10.1016/S2542-5196(19)30046-4), 2019.
- Akimoto, H.: Overview of policy actions and observational data for PM_{2.5} and O₃ in Japan: a study of urban air quality improvement in Asia, JICA-RI Working Paper, 137, 2017.
- 650 Barré, J., Petetin, H., Colette, A., Guevara, M., Peuch, V.-H., Rouil, L., Engelen, R., Inness, A., Flemming, J., Pérez Garcia-Pando, C., Bowdalo, D., Meleux, F., Geels, C., Christensen, J. H., Gauss, M., Benedictow, A., Tsyro, S., Friese, E., Struzewska, J., Kaminski, J. W., Douros, J., Timmermans, R., Robertson, L., Adani, M., Jorba, O., Joly, M., and Kouznetsov, R.: Estimating lockdown-induced European NO₂ changes using satellite and surface observations and air quality models, *Atmos. Chem. Phys.*, 21, 7373–7394, <https://doi.org/10.5194/acp-21-7373-2021>, 2021.
- 655 Bauwens, M., Comperolle, S., Stavrakou, T., Müller, J.-F., van Gent, J., Eskes, H., et al.: Impact of coronavirus outbreak on NO₂ pollution assessed using TROPOMI and OMI observations. *Geophysical Research Letters* 47, e2020GL087978. <https://doi.org/10.1029/2020GL087978>, 2020.
- Beirle, S., Borger, C., Dörner, S., Li, A., Hu, Z., Liu, F., Wang, Y. and Wagner, T.: Pinpointing nitrogen oxide emissions from space, *Sci. Adv.* 5(11). doi:10.1126/sciadv.aax9800, 2019.
- 660 Beirle, S., Platt, U., Wenig, M. & Wagner, T.: Weekly cycle of NO₂ by GOME measurements: a signature of anthropogenic sources. *Atmos. Chem. Phys.* 3, 2225–2232, 2003.

- Brancher, M.: Increased ozone pollution alongside reduced nitrogen dioxide concentrations during Vienna's first COVID-19 lockdown: Significance for air quality management, *Environmental Pollution*, 284, 117153, <https://doi.org/10.1016/j.envpol.2021.117153>, 2021.
- 665 Cleveland, W.S., Graedel, T.E., Kleiner, B. and Warner, J.L.: Sunday and workday variations in photochemical air pollutants in New Jersey and New York. *Science* 186, 1037–1038. doi:10.1080/10473289.2003.10466222, 1974.
- Cooper, M. J., Martin, R. V., Hammer, M. S., Levelt, P. F., Veefkind, P., Lamsal, L. N., Krotkov, N. A., Brook, J. R. and McLinden, C. A.: Global fine-scale changes in ambient NO₂ during COVID-19 lockdowns, *Nature*, 601, 380-387, doi:10.1038/s41586-021-04229-0, 2022.
- 670 [Compernelle, S., Verhoelst, T., Pinardi, G., Granville, J., Hubert, D., Keppens, A., Niemeijer, S., Rino, B., Bais, A., Beirle, S., Boersma, F., Burrows, J. P., De Smedt, I., Eskes, H., Goutail, F., Hendrick, F., Lorente, A., Pazmino, A., PETERS, A., Peters, E., Pommereau, J.-P., Remmers, J., Richter, A., van Geffen, J., Van Roozendael, M., Wagner, T., and Lambert, J.-C.: Validation of Aura-OMI QA4ECV NO₂ climate data records with ground-based DOAS networks: the role of measurement and comparison uncertainties. *Atmos. Chem. Phys.*, 20, 8017–8045, <https://doi.org/10.5194/acp-20-8017-2020>, 2020.](#)
- 675 Damiani, A., Irie, H., Yamaguchi, K., Hoque, H. M. S., Nakayama, T., Matsumi, Y., Kondo, Y., and Da Silva, A.: Variabilities in PM_{2.5} and black carbon surface concentrations reproduced by aerosol optical properties estimated by in-situ data, ground based remote sensing and modeling, *Remote Sens.*, 13, 3163, <https://doi.org/10.3390/rs13163163>, 2021.
- De Smedt, I., Pinardi, G., Vigouroux, C., Compernelle, S., Bais, A., Benavent, N., Boersma, F., Chan, K.-L., Donner, S., Eichmann, K.-U., Hedelt, P., Hendrick, F., Irie, H., Kumar, V., Lambert, J.-C., Langerock, B., Lerot, C., Liu, C., Loyola, D.,
- 680 [Peters, A., Richter, A., Rivera Cárdenas, C., Romahn, F., Ryan, R. G., Sinha, V., Theys, N., Vlietinck, J., Wagner, T., Wang, T., Yu, H., and Van Roozendael, M.: Comparative assessment of TROPOMI and OMI formaldehyde observations and validation against MAX-DOAS network column measurements, *Atmos. Chem. Phys.*, 21, 12561–12593, <https://doi.org/10.5194/acp-21-12561-2021>, 2021.](#)
- De Smedt, I., Theys, N., Yu, H., Danckaert, T., Lerot, C., Compernelle, S., Van Roozendael, M., Richter, A., Hilboll, A.,
- 685 [Peters, E., Pedergrana, M., Loyola, D., Beirle, S., Wagner, T., Eskes, H., van Geffen, J., Boersma, K. F., and Veefkind, P.: Algorithm theoretical baseline for formaldehyde retrievals from S5P TROPOMI and from the QA4ECV project, *Atmos. Meas. Tech.*, 11, 23952426, <https://doi.org/10.5194/amt-11-2395-2018>, 2018.](#)
- Duncan, B. N., Yoshida, Y., Olson, J. R., Sillman, S., Martin, R. V., Lamsal, L., Hu, Y. T., Pickering, K. E., Retscher, C., Allen, D. J., and Crawford, J. H.: Application of OMI observations to a space-based indicator of NO_x and VOC controls on
- 690 surface ozone formation, *Atmos. Environ.*, 44, 2213–2223, <https://doi.org/10.1016/j.atmosenv.2010.03.010>, 2010.
- 695 [Geddes, J.A., Martin, R.V., Boys, B.L., van Donkelaar, A.: Long-term trends worldwide in ambient NO₂ concentrations inferred from satellite observations, *Environ Health Perspect*, 124, 281–289, <http://dx.doi.org/10.1289/ehp.1409567>, 2016.](#)
- [Georgoulias, A. K., van der A, R. J., Stammes, P., Boersma, K. F., and Eskes, H. J.: Trends and trend reversal detection in 2 decades of tropospheric NO₂ satellite observations, *Atmos. Chem. Phys.*, 19, 6269–6294, <https://doi.org/10.5194/acp-19-6269-2019>, 2019.](#)

Ghahremanloo, M., Lops, Y., Choi, Y., Mousavinezhad, S.: Impact of the COVID-19 outbreak on air pollution levels in East Asia, *Science of The Total Environment*, 754, 142226, ISSN 0048-9697, <https://doi.org/10.1016/j.scitotenv.2020.142226>, 2021.

700 Gkatzelis G. I., Gilman, J. B., Brown, S. S., Eskes, H., Gomes, A. R., Lange, A. C., McDonald, B. C., Peischl, J., Petzold, A., Thompson, C. R., and Kiendler-Scharr, A.: The global impacts of COVID-19 lockdowns on urban air pollution: A critical review and recommendations, *Elementa: Science of the Anthropocene*, 9,1: 00176, <https://doi.org/10.1525/elementa.2021.00176>, 2021.

Guevara M., Jorba, O., Soret, A., Petetin, H., Bowdalo, D., Serradell, K., Tena, C., Denier van der Gon, H., Kuenen, J., Peuch, V.-H., Pérez García-Pando, C.: Time-resolved emission reductions for atmospheric chemistry modelling in Europe during the COVID-19 lockdowns, *Atmos. Chem. Phys.*, 21, 773-797, 10.5194/acp-21-773-2021, 2021.

705 Hamra, G. B., Laden, F., Cohen, A. J., Raaschou-Nielsen, O., Brauer, M., & Loomis, D.: Lung Cancer and Exposure to Nitrogen Dioxide and Traffic: A Systematic Review and Meta-Analysis, *Environmental health perspectives*, 123, 11, 1107–1112, <https://doi.org/10.1289/ehp.1408882>, 2015.

Hönninger, G., Von Friedeburg, C., Platt, U.: Multi axis differential optical absorption spectroscopy (MAX-DOAS), *Atmos. Chem. Phys.*, 4, 231–254, 2004.

710 Ialongo, I., Virta, H., Eskes, H., Hovila, J., and Douros, J.: Comparison of TROPOMI/Sentinel-5 Precursor NO₂ observations with ground-based measurements in Helsinki, *Atmos. Meas. Tech.*, 13, 205–218, <https://doi.org/10.5194/amt-13-205-2020>, 2020.

Inness, A., Ades, M., Agustí-Panareda, A., Barré, J., Benedictow, A., Blechschmidt, A.-M., Dominguez, J. J., Engelen, R., Eskes, H., Flemming, J., Huijnen, V., Jones, L., Kipling, Z., Massart, S., Parrington, M., Peuch, V.-H., Razinger, M., Remy, S., Schulz, M., and Suttie, M.: The CAMS reanalysis of atmospheric composition, *Atmos. Chem. Phys.*, 19, 3515–3556, <https://doi.org/10.5194/acp-19-3515-2019>, 2019.

715 Irie, H., Takashima, H., Kanaya Y., Boersma, K.F., Gast, L., Wittrock, F., Brunner, D., Zhou, Y., Van Roozendaal, M.: Eight-component retrievals from ground-based MAX-DOAS observations, *Atmos. Meas. Tech.*, 4, 6, 1027–1044, <https://doi.org/10.5194/amt-4-1027-2011>, 2011.

720 Irie, H., Yonekawa, D., Damiani, A., Hoque, H. M. S., Sudo, K., and Itahashi, S.: Continuous multi-component MAX-DOAS observations for the planetary boundary layer ozone variation analysis at Chiba and Tsukuba, Japan, from 2013 to 2019, *Prog. Earth Planet. Sci.*, 8, 31, 2021.

Irie, H., Nakayama, T., Shimizu, A., Yamazaki, A., Nagai, T., Uchiyama, A., Zaizen, Y., Kagamitani, S., Matsumi, Y., Evaluation of MAX-DOAS aerosol retrievals by coincident observations using CRDS, lidar, and sky radiometer in Tsukuba, Japan, *Atmos. Meas. Tech.*, 8, 2775–2788, 2015.

Itahashi, S., Yamamura, Y., Wang, Z. et al. Returning long-range PM_{2.5} transport into the leeward of East Asia in 2021 after Chinese economic recovery from the COVID-19 pandemic. *Sci Rep* 12, 5539, <https://doi.org/10.1038/s41598-022-09388-2>, 2022.

- 730 Jin, X., Fiore, A. M., Murray, L. T., Valin, L. C., Lamsal, L. N., Duncan, B., Boersma, K.F., De Smedt, I., Abad, G.G., Chance, K., and Tonnesen, G.: Evaluating a space-based indicator of surface ozone-NO_x-VOC sensitivity over midlatitude source regions and application to decadal trends, *J. Geophys. Res.*, 122(19), 10,439-410,461, <https://doi.org/10.1002/2017JD026720>, 2017.
- Ju, M. J., Oh, J., Choi, Y. H.: Changes in air pollution levels after COVID-19 outbreak in Korea, *Science of the Total Environment* 750, 141521, <https://doi.org/10.1016/j.scitotenv.2020.141521>, 2021.
- 735 Kondo, Y., Sahu, L., Kuwata, M., Miyazaki, Y., Takegawa, N., Moteki, N., Imaru, J., Han, S., Nakayama, T., Kim, O.N.T., et al.: Stabilization of the mass absorption cross section of black carbon for filter-based absorption photometry by the use of a heated inlet, *Aerosol Sci. Technol.*, 43, 741–756, 2009.
- Kurokawa, J. and Ohara, T.: Long-term historical trends in air pollutant emissions in Asia: Regional Emission inventory in ASia (REAS) version 3, *Atmos. Chem. Phys.*, 20, 12761–12793, <https://doi.org/10.5194/acp-20-12761-2020>, 2020
- 740 Lamsal, L. N., Krotkov, N. A., Vasilkov, A., Marchenko, S., Qin, W., Yang, E.-S., Fasnacht, Z., Joiner, J., Choi, S., Haffner, D., Swartz, W. H., Fisher, B., and Bucsela, E.: Ozone Monitoring Instrument (OMI) Aura nitrogen dioxide standard product version 4.0 with improved surface and cloud treatments, *Atmos. Meas. Tech.*, 14, 455–479, <https://doi.org/10.5194/amt-14-455-2021>, 2021.
- 745 Laughner J. L. et al., Societal shifts due to COVID-19 reveal large-scale complexities and feedbacks between atmospheric chemistry and climate change, 118 (46) e2109481118, <https://doi.org/10.1073/pnas.2109481118>, 2021.
- Le, T., Wang, Y., Liu, L., Yang, J., Yung, Y. L., Li, G., Seinfeld, J. H.: Unexpected air pollution with marked emission reductions during the COVID-19 outbreak in China. *Science*, 369(6504):702-706. doi: 10.1126/science.abb7431, 2020.
- Lee, H.-J., Chang, L.-S., Jaffe, D.A., Bak, J., Liu, X., Abad, G.G., Jo, H.-Y., Jo, Y.-J., Lee, J.-B., Kim, C.-H.: Ozone 750 Continues to Increase in East Asia Despite Decreasing NO₂: Causes and Abatements, *Remote Sensing*, 13, 11, 2177, <https://doi.org/10.3390/rs13112177>, 2021.
- Li, K., Jacob, D. J., Liao, H., Shen, L., Zhang, Q., Bates, K. H.: Anthropogenic drivers of 2013–2017 trends in summer surface ozone in China, *Proc Natl Acad Sci USA.*, 116:422–7, doi: 10.1073/pnas.1812168116, 2019.
- Liu, Y., Wang, T., Stavrakou, T., Elguindi, N., Doumbia, T., Granier, C., Bouarar, I., Gaubert, B., Brasseur, G. P.: Diverse 755 response of surface ozone to COVID-19 lockdown in China, *Science of the Total Environment*, 789, 147739, <https://doi.org/10.1016/j.scitotenv.2021.147739>, 2021.
- Liu, F., Beirle, S., Zhang, Q., Dörner, S., He, K., and Wagner, T.: NO_x lifetimes and emissions of cities and power plants in polluted background estimated by satellite observations, *Atmos. Chem. Phys.*, 16, 5283–5298, <https://doi.org/10.5194/acp-16-5283-2016>, 2016.
- 760 Martin, R. V., Fiore, A. M., and Van Donkelaar, A.: Space-based diagnosis of surface ozone sensitivity to anthropogenic emissions, *Geophys. Res. Lett.*, 31, L06120, doi: 10.1029/2004GL019416, 2004.

- Murphy, J. G., Day, D. A., Cleary, P. A., Wooldridge, P. J., Millet, D. B., Goldstein, A. H., and Cohen, R. C.: The weekend effect within and downwind of Sacramento – Part 1: Observations of ozone, nitrogen oxides, and VOC reactivity, *Atmos. Chem. Phys.*, 7, 5327–5339, <https://doi.org/10.5194/acp-7-5327-2007>, 2007.
- 765 Miyazaki, K., Bowman, K., Sekiya, T., Takigawa, M., NeuI, J. L., Sudo, K., Osterman, G., Eskes, H.: Global tropospheric ozone responses to reduced NO_x emissions linked to the COVID-19 worldwide lockdowns, *Science Advances*, 7, 24, doi: 10.1126/sciadv.abf7460, 2021.
- Nouvellet, P., Bhatia, S., Cori, A. et al.: Reduction in mobility and COVID-19 transmission, *Nat. Commun.*, 12, 1090, <https://doi.org/10.1038/s41467-021-21358-2>, 2021.
- 770 Petetin, H., Thouret, V., Athier, G., Blot, R., Boulanger, D., Cousin, J.-M., Gaudel, A., Nédélec, P., Cooper, O.: Diurnal cycle of ozone throughout the troposphere over Frankfurt as measured by MOZAIC-IAGOS commercial aircraft, *Elem. Sci. Anth.*, 4, 129, 2016.
- Platt, U., and Stutz, J.: *Differential optical absorption spectroscopy, principles and applications*, Springer, XV, 597 p. 272 illus., 29 in color, *Physics of Earth and Space Environments*, ISBN 978-3-540-21193-8, 2008.
- 775 Russell, A. R., Valin, L. C., and Cohen, R. C.: Trends in OMI NO₂ observations over the United States: effects of emission control technology and the economic recession, *Atmos. Chem. Phys.*, 12, 12197–12209, <https://doi.org/10.5194/acp-12-12197-2012>, 2012.
- Sadanaga, Y., Sengen, M., Takenaka, N. and Bandow, H.: Analyses of the Ozone Weekend Effect in Tokyo, Japan: Regime of Oxidant (O₃ + NO₂) Production, *Aerosol Air Qual. Res.*, 12, 161-168, <https://doi.org/10.4209/aaqr.2011.07.0102>, 2012.
- 780 Shakil, M. H., Munim, ZH, Tasnia, M, Sarowar, S.: COVID-19 and the environment: A critical review and research agenda. *Science of the Total Environment* 745. DOI: <http://dx.doi.org/10.1016/j.scitotenv.2020.141022>, 2020.
- Shen, L., Jacob, D. J., Liu, X., Huang, G., Li, K., Liao, H., and Wang, T.: An evaluation of the ability of the Ozone Monitoring Instrument (OMI) to observe boundary layer ozone pollution across China: application to 2005–2017 ozone trends, *Atmos. Chem. Phys.*, 19, 6551–6560, <https://doi.org/10.5194/acp-19-6551-2019>, 2019.
- 785 Sicard P., Paoletti, E., Agathokleous, E., Araminienè, V., Proietti, C., Coulibaly, F., De Marco, A.: Ozone weekend effect in cities: Deep insights for urban air pollution control, *Environmental Research*, 191, 110193, <https://doi.org/10.1016/j.envres.2020.110193>, 2020a.
- Sicard P., De Marco, A., Agathokleous, E., Feng, Z., Xu, X., Paoletti, E., Diéguez Rodriguez, J. J., Calatayud, V.: Amplified ozone pollution in cities during the COVID-19 lockdown, *Science of The Total Environment*, 735, 139542, 2020b.
- 790 Sillman, S.: The use of NO_y, H₂O₂, and HNO₃ as indicators for Ozone-NO_x-Hydrocarbon sensitivity in urban Locations, *J. Geophys. Res. Atmos.*, 100, 14175–14188, <https://doi.org/10.1029/94jd02953>, 1995
- Stavrakou, T., Müller, J.-f., Bauwens, M., Boersma K. f. & van Geffen, J.: Satellite evidence for changes in the no₂ weekly cycle over large cities. *Scientific Reports* 10:10066, <https://doi.org/10.1038/s41598-020-66891-0>, 2020.

- Steinbrecht, W., Kubistin, D., Plass-Dülmer, C., Davies, J., Tarasick, D. W., Gathen, P., et al.: COVID-19 crisis reduces free tropospheric ozone across the Northern Hemisphere, *Geophysical Research Letters*, 48, e2020GL091987, <https://doi.org/10.1029/2020GL091987>, 2021.
- Sugawara, H., Ishidoya, S., Terao, Y., Takane, Y., Kikegawa, Y., and Nakajima, K.: Anthropogenic CO₂ emissions changes in an urban area of Tokyo, Japan, due to the COVID-19 pandemic: A case study during the state of emergency in April–May 2020, *Geophysical Research Letters*, 48, e2021GL092600, <https://doi.org/10.1029/2021GL092600>, 2021.
- 800 Sun, W., Zhu, L., De Smedt, I., Bai, B., Pu, D., Chen, Y., et al.: Global significant changes in formaldehyde (HCHO) columns observed from space at the early stage of the COVID-19 pandemic. *Geophysical Research Letters*, 48, e2020GL091265, <https://doi.org/10.1029/2020GL091265>, 2021.
- Surl, L., Palmer, P. I., and González Abad, G.: Which processes drive observed variations of HCHO columns over India?, *Atmos. Chem. Phys.*, 18, 4549–4566, <https://doi.org/10.5194/acp-18-4549-2018>, 2018.
- 805 Tan, P.-H., Chou, C., Liang, J.-Y., Chou, C. C.-K., Shiu, C.-J.: Air pollution “holiday effect” resulting from the Chinese New Year, *Atmospheric Environment*, 43, 2114–2124, ISSN 1352-2310, <https://doi.org/10.1016/j.atmosenv.2009.01.037>, 2009.
- Takane, Y., Nakajima, K., and Kikegawa, Y.: Urban climate changes during the COVID-19 pandemic: integration of urban-building-energy model with social big data, *npj Clim Atmos Sci* 5, 44, <https://doi.org/10.1038/s41612-022-00268-0>, 2022.
- 810 Takashima, H., Irie, H., Kanaya, Y., Shimizu, A., Aoki, K., Akimoto, H.: Atmospheric aerosol variations at Okinawa Island in Japan observed by MAX-DOAS using a new cloud screening method, *J Geophys Res* 114(D18):D18213, <https://doi.org/10.1029/2009JD011939>, 2009.
- van Geffen, J. H. G. M., et al.: TROPOMI ATBD of the total and tropospheric NO₂ data products. Report S5P-KNMI-L2-0005-RP, KNMI, De Bilt, The Netherlands, 2021.
- 815 van Stratum, B. J. H., Vilà-Guerau de Arellano, J., Ouwersloot, H. G., van den Dries, K., van Laar, T. W., Martinez, M., Lelieveld, J., Dirsch, J.-M., Drewnick, F., Fischer, H., Hosaynali Beygi, Z., Harder, H., Regelin, E., Sinha, V., Adame, J. A., Sörgel, M., Sander, R., Bozem, H., Song, W., Williams, J., and Yassaa, N.: Case study of the diurnal variability of chemically active species with respect to boundary layer dynamics during DOMINO, *Atmos. Chem. Phys.*, 12, 5329–5341, <https://doi.org/10.5194/acp-12-5329-2012>, 2012.
- 820 Veeffkind, J. P., Aben, I., McMullan, K., Förster, H., de Vries, J., Otter, G., Claas, J., Eskes, H. J., de Haan, J. F., Kleipool, Q., van Weele, M., Hasekamp, O., Hoogeveen, R., Landgraf, J., Snel, R., Tol, P., Ingmann, P., Voors, R., Kruizinga, B., and Vink, R.: TROPOMI on the ESA Sentinel-5 Precursor: A GMES mission for global observations of the atmospheric composition for climate, air quality and ozone layer applications, *Remote Sens. Environ.*, 120, 70–83, 2012.
- Verhoelst, T., et al.: Ground-based validation of the Copernicus Sentinel-5P TROPOMI NO₂ measurements with the NDACC ZSL-DOAS, MAX-DOAS and Pandonia global networks, *Atmos. Meas. Tech.*, 14, 481–510, <https://doi.org/10.5194/amt-14-481-2021>, 2021.

Vilà-Guerau de Arellano, J., van Heerwaarden, C.C., van Stratum, B.J., van den Dries, K.: Atmospheric Boundary Layer: Integrating Chemistry and Land Interactions, Cambridge University Press, New York, USA, p. 265, 2015.

Vohra, K., Marais, E. A., Bloss, W. J., Schwartz, J., Mickley, L. J., Van Damme, M., Clarisse, L., Coheur, P. F.: Rapid rise
830 in premature mortality due to anthropogenic air pollution in fast-growing tropical cities from 2005 to 2018, *Science Advances*, 8, 14, DOI: 10.1126/sciadv.abm4435, 2022.

Venter, Z. S., Aunan, K., Chowdhury, S., Lelieveld, J.: COVID-19 lockdowns cause global air pollution declines. *Proceedings of the National Academy of Sciences* 117 (32) 18984-18990. DOI: 10.1073/pnas.2006853117, 2020.

Zara, M., Boersma, K. F., Eskes, H., Denier van der Gon, H., Vilà-Guerau de Arellano, J., Krol, M., van der Swaluw, E.,
835 Schuch, W., Velders, G. J.M.: Reductions in nitrogen oxides over the Netherlands between 2005 and 2018 observed from space and on the ground: Decreasing emissions and increasing O₃ indicate changing NO_x chemistry, *Atmospheric Environment: X*, 9, 1-12, <https://doi.org/10.1016/j.aeaoa.2021.100104>, 2021.

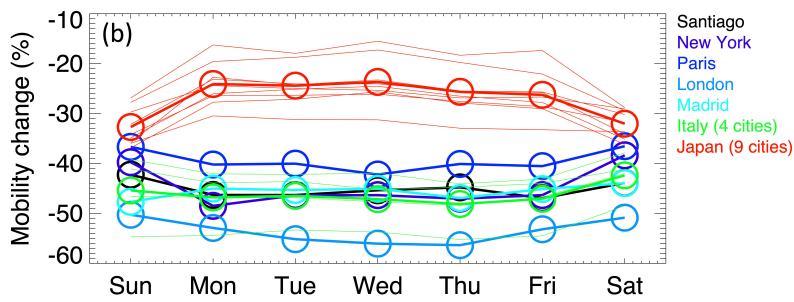
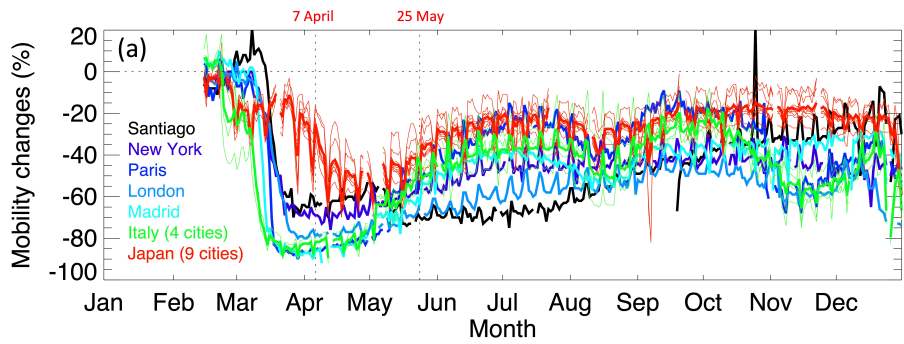
Ziemke, J. R., Oman, L. D., Strode, S. A., Douglass, A. R., Olsen, M. A., McPeters, R. D., Bhartia, P. K., Froidevaux, L., Labow, G. J., Witte, J. C., Thompson, A. M., Haffner, D. P., Kramarova, N. A., Frith, S. M., Huang, L.-K., Jaross, G. R.,
840 Seftor, C. J., Deland, M. T., and Taylor, S. L.: Trends in global tropospheric ozone inferred from a composite record of TOMS/OMI/MLS/OMPS satellite measurements and the MERRA-2 GMI simulation, *Atmos. Chem. Phys.*, 19, 3257–3269, <https://doi.org/10.5194/acp-19-3257-2019>, 2019.

Zou, Y., Charlesworth, E., Yin, C.Q., Yan, X.L., Deng, X.J., Li, F.: The weekday/weekend ozone differences induced by the emissions change during summer and autumn in Guangzhou, China, *Atmospheric Environment*, 199, 114-126, ISSN 1352-
845 2310, <https://doi.org/10.1016/j.atmosenv.2018.11.019>, 2019.

850

855

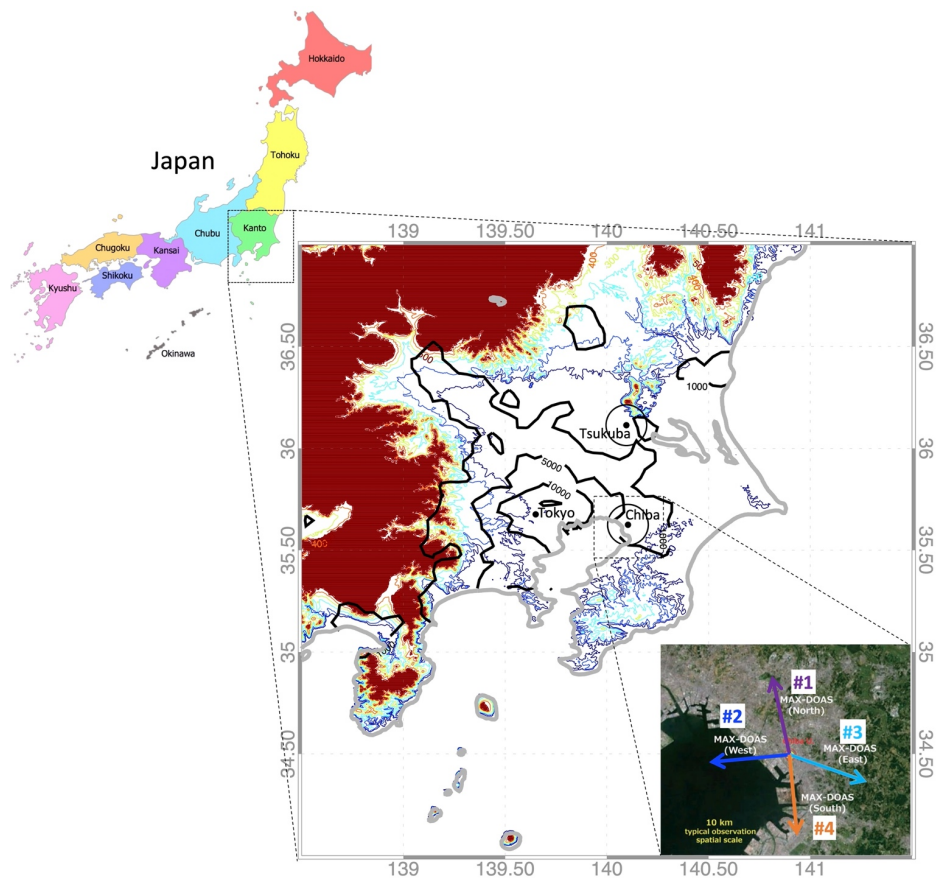
860



865 Figure 1: Google mobility data for the place category Transit stations in 2020 (from February 15 to December 31) compared to the pre-COVID period, for selected large metropolitan areas around the world strongly affected by the pandemic. For Japan and Italy, values were averaged (thick line) over 9 (Tokyo, Kanagawa, Saitama, Chiba, Kyoto, Nara, Osaka, Fukuoka, Nagasaki) and 4 (Milan, Rome, Naples and Turin) cities/prefectures (thin lines), respectively: (a) time series; (b) weekly changes. Holidays were removed. The baseline in both panel (a) and panel (b) is the median value for the corresponding day of the week during the 5-week period of January 3–February 6, 2020.

870

875



880 **Figure 2:** Main panel: Terrain map (meters above sea level, colored isolines; elevations > 0.5 km shaded dark red) from the General Bathymetric Chart of the Oceans (GEBCO) 2021 and population density (black isolines, people/km²) from the Gridded Population of the World, Version 4 (GPWv4). Circles highlight the average area sampled by the MAX-DOAS system (four azimuthal directions for Chiba, one direction for Tsukuba). The top inset shows the location of the investigated Kanto region in Japan and the bottom inset (© Google Maps 2019) shows the azimuthal pointing directions of the four MAX-DOAS systems deployed at Chiba University.

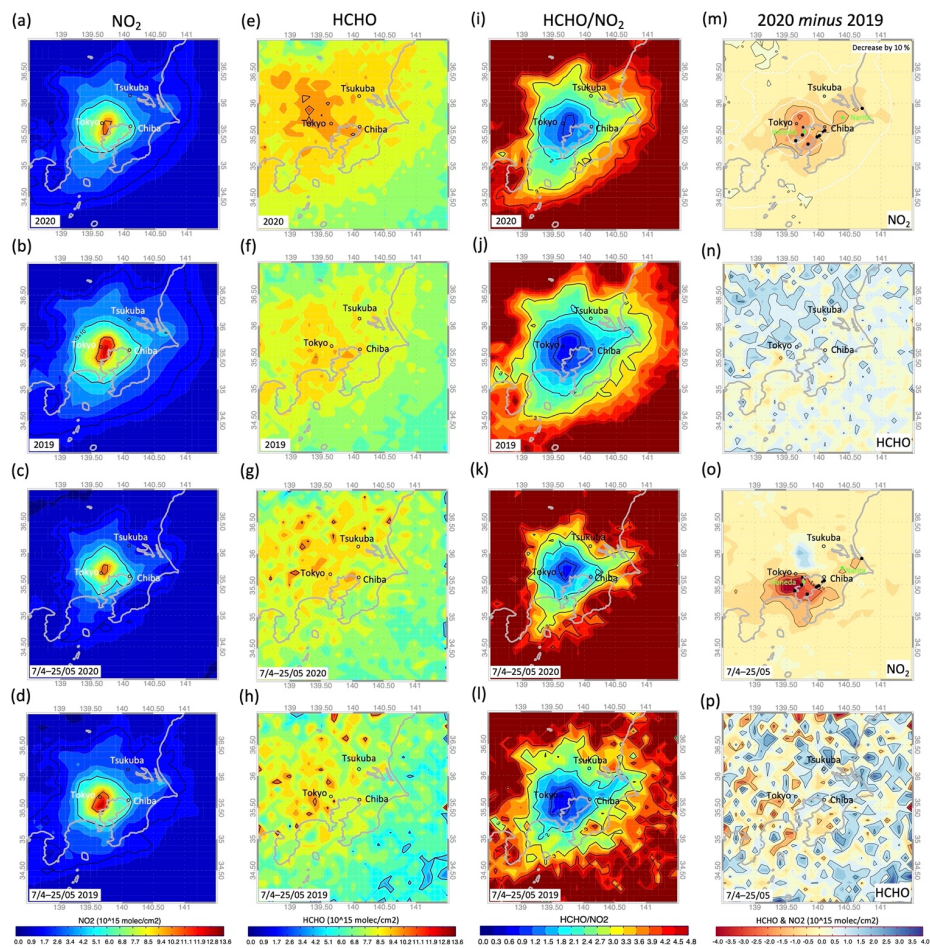
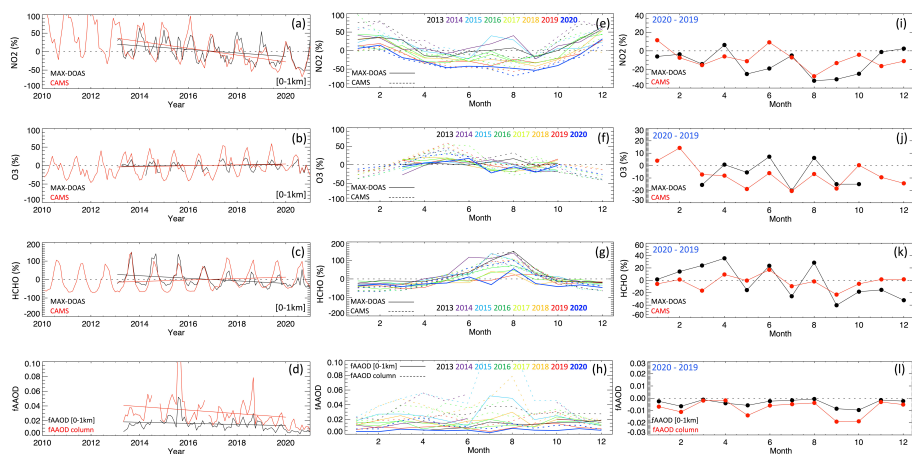
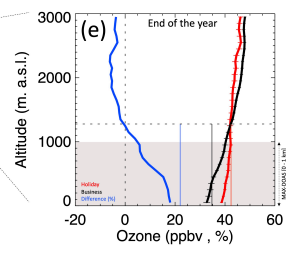
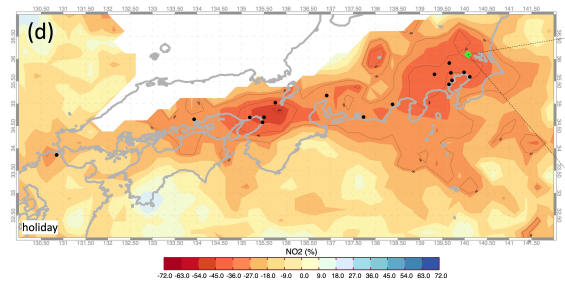
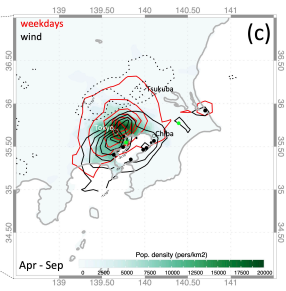
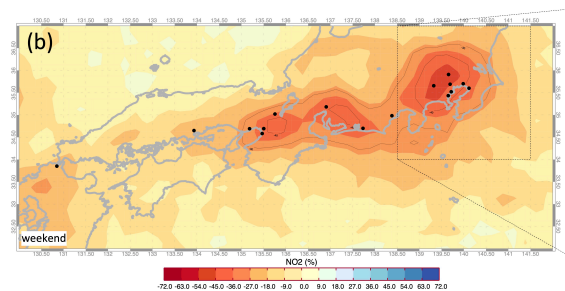
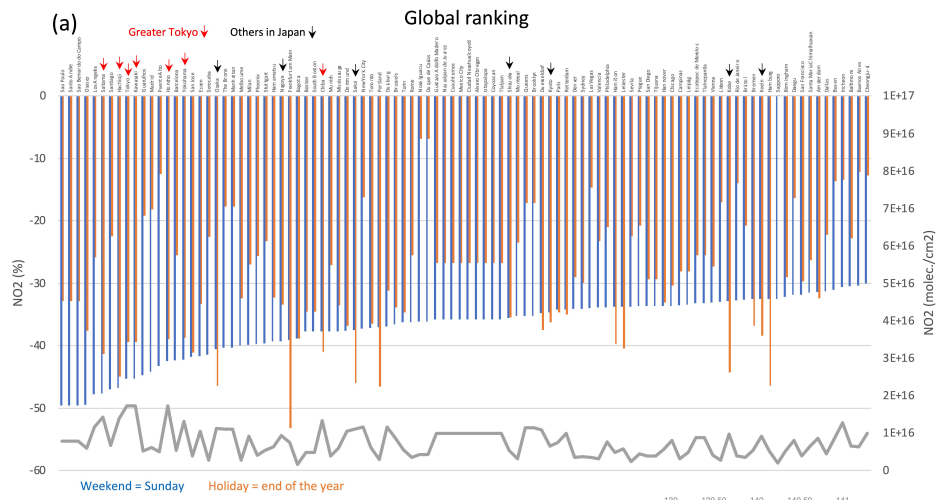


Figure 3: Top two panels: Spatial distribution of TROPOMI NO_2 (a,b), HCHO (e,f), and HCHO/ NO_2 (i,j) in 2020 and 2019, as well as the 2020–2019 differences in NO_2 (m) and HCHO (n). Bottom two panels: Spatial distribution of TROPOMI observations as described above but limited to 7 April–25 May (i.e., the state of emergency).

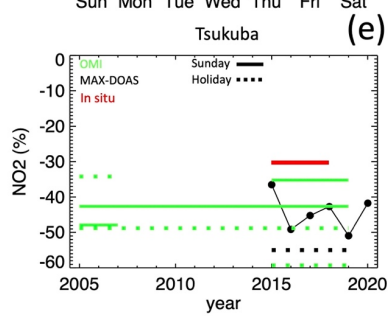
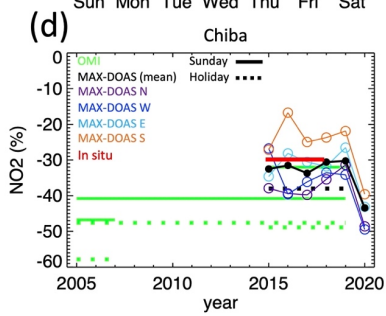
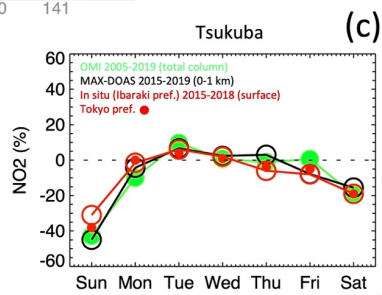
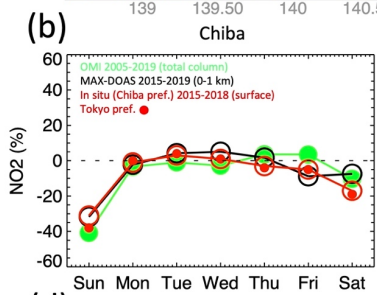
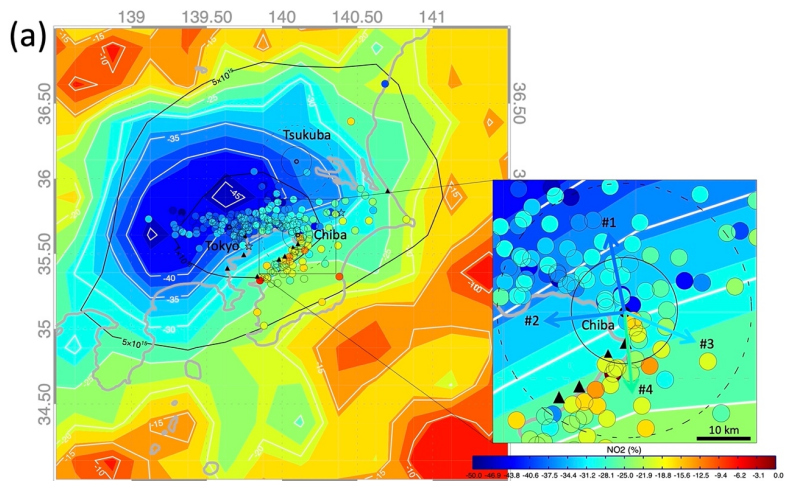


895 **Figure 4:** Left column: monthly time series of NO₂ (a), O₃ (b), and HCHO (c) partial tropospheric column (< 1 km) as recorded by the MAX-DOAS system and estimated by CAMS at Chiba University. Central column: seasonal monthly changes in MAX-DOAS observations and CAMS estimates of NO₂ (e), O₃ (f) and HCHO (g). Right column: differences (2020 minus 2019) in MAX-DOAS observations and CAMS estimates for NO₂ (i), O₃ (j) and HCHO (k). Results are shown as percentage changes with respect to the 2013–2019 average (left and central panels) and 2019 (right panel). Bottom panel: changes as described above but for fine mode light-absorbing aerosols i.e., fAOD and fAOD (0–1 km).



900 Figure 5: Global ranking of the weekend effect (Sunday minus weekdays, blue) and holiday effect (end-of-year period minus
business days, orange) for cities with a population greater than 0.5 million based on OMI NO₂ in 2005–2019. Only cities where
changes were larger than 30% were shown. Opposite axis: mean NO₂; total tropospheric column in grey (a). The spatial
distribution of the weekend effect over Japan ((b), relative changes) and over the Kanto region ((c), absolute changes limited to
905 April–September. Red lines: Sunday minus weekdays; black points: power plants; green points: airports). Wind-related NO₂
changes limited to April–September (black lines: high minus low wind speed) and population density (filled contours, in green
shades) are also plotted in (c). Contours for both red and black solid lines read as follows: -1,-2,-3,-4,-5,-6 x10¹⁵ molec./cm². Then,
the black dashed lines show positive changes (0.5, 1 x10¹⁵ molec./cm²). Spatial distribution of the holiday effect in NO₂ across
Japan (d); the low number of OMI observations prevents determination of the difference along the coastline of the Japan Sea.
910 Ozone profiles obtained from ozonesondes launched from Tateno (green point in (d)) during the end-of-year holiday period and
business holidays in 2013–2020 (i.e., when MAX-DOAS data were available) are plotted along with box simulations (vertical lines)
of the mean ozone concentration within the boundary layer (e). See Sect. 2 for further details.

Deleted:



915 Figure 6: Spatial distribution of the weekend effect (Sunday minus weekdays) based on OMI NO₂ total tropospheric column (filled
| contours), MAX-DOAS partial [tropospheric column](#) (< 1 km, colored arrows), and in situ NO₂ observations (circles) over 2015–
2018 ((a), main panel). Magnified view of the area around Chiba University (inset). NO₂ weekly cycle at Chiba and Tsukuba for
920 the datasets noted above. In situ data were averaged across the prefecture (b,c). The weekend effect (on Sunday) and the holiday
effect (at the end of the year) were averaged over different periods (as indicated by the horizontal lines) at Chiba and Tsukuba
(d,e). MAX-DOAS NO₂ data are also plotted for each year and for each instrument at Chiba.

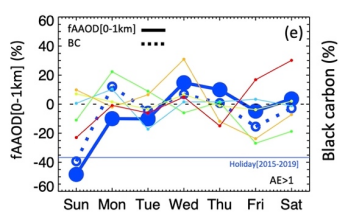
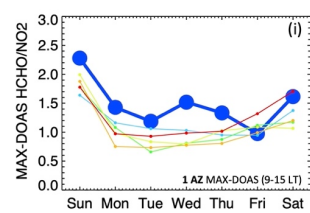
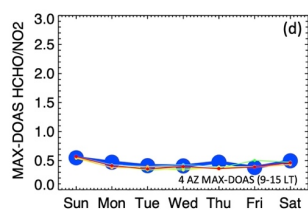
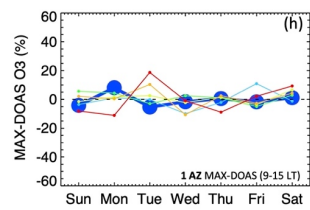
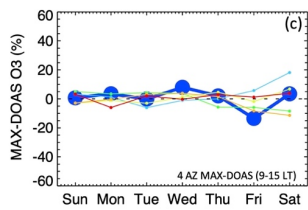
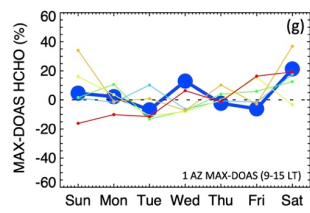
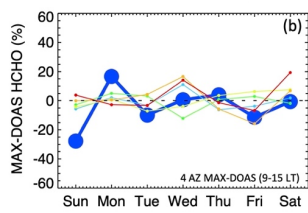
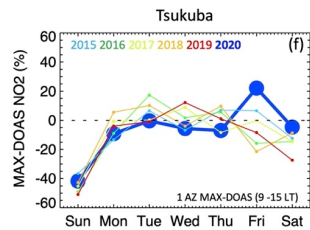
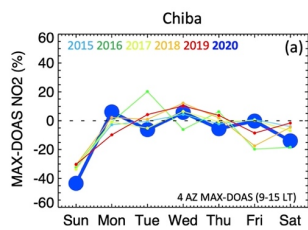


Figure 7: Weekly changes in MAX-DOAS partial tropospheric column (top to bottom) NO₂, HCHO, O₃, HCHO/NO₂, and fAAOD for Chiba (right) and Tsukuba (left) during 2015–2020. Only data with SZA < 50 were considered in the O₃ dataset; see text for details. Panel (e) includes the weekly cycle of surface BC concentrations. BC data were unavailable for Tsukuba.

930

935

940

945

950

955

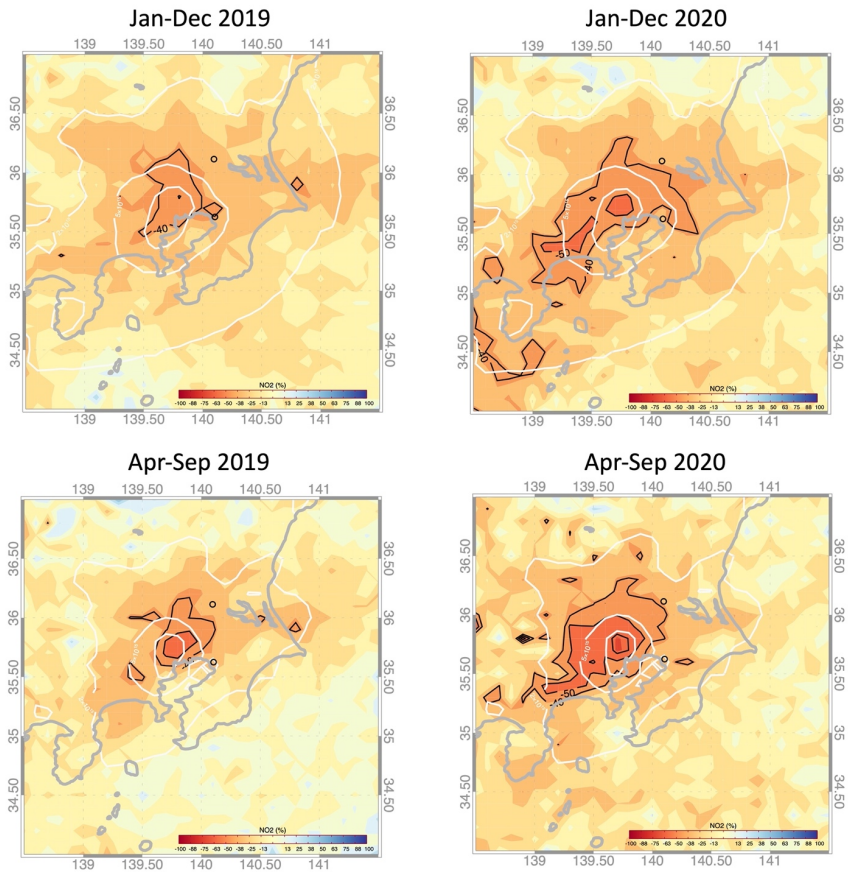


Figure 8: Spatial distribution of the TROPOMI NO₂ weekend effect (Sunday minus weekdays) in January to December 2019 (a), January to December 2020 (b), April to September 2019 (c), and April to September 2020 (d).